ChemComm



FEATURE ARTICLE

View Article Online



Cite this: Chem. Commun., 2017, **53** 4653

Received 25th November 2016, Accepted 30th March 2017

DOI: 10.1039/c6cc09421i

rsc.li/chemcomm

Molecular imaging probes for multi-spectral optoacoustic tomography†

Vipul Guirati.

Anurag Mishra

and Vasilis Ntziachristos

**Above Anurag Mishra

Data and Vasilis Ntziachristos

**Para Ntziachristos

Data and Vasilis Ntziachristos

Data and Vasilis Ntziachristos

**Para Ntziachristos

Data and Vasilis Ntziachristos

**Para Ntziachristos

Data and Vasilis Ntziachristos

**Para Ntziachristos

Multi-Spectral Optoacoustic Tomography (MSOT) merges the power of high-resolution imaging at tissue depths of several millimeters to centimeters with the advantages of optical imaging, in large part by exploiting spectral detection of endogenous molecules in tissue or exogenous photoabsorbing probes. Current advances in fast-tuning laser technology, image reconstruction and spectral detection schemes have yielded real-time optoacoustic (photoacoustic) imaging spanning applications from microscopy to human imaging. This progress has generated an unprecedented need for imaging probes and reporter gene approaches optimized for optoacoustic signal generation. New classes of probes are emerging and create new opportunities for visualizing morphological and pathophysiological features in vivo, in a noninvasive manner. Here we review recent progress in optoacoustic probes and discuss applications and challenges for biological imaging as well as prospects for clinical translation.

[†] We thank the Deutsche Forschungsgemeinschaft, Germany: Gottfried Wilhelm Leibniz Prize 2013; NT 3/10-1 and Cluster of Excellence Nanosystems Initiative Munich (VG and VN), and the HMGU ERC recognition award (AM). We also thank Dr A. Chapin Rodriguez for proofreading support.



Vipul Gujrati

Vipul Gujrati received his Master's in Pharmacy in 2006 from the Rajiv Gandhi University of Health Sciences in India, after which he worked as a research scientist at Torrent Pharmaceuticals LTD in India. From 2010 to 2014, he completed a PhD on the development of bioengineered drug delivery nanocarriers under the guidance of Prof. Dr Sangyong Jon at the Gwangju Institute of Science and Technology (GIST) and Korea Advanced Institute of Science and

Technology (KAIST) in South Korea, where he stayed on as a postdoctoral researcher. In May 2016 he joined the group of Prof. Dr Vasilis Ntziachristos at the Institute for Biological and Medical Imaging (IBMI) at the Technical University of Munich (TUM), Germany, as a postdoctoral fellow. At IBMI he is developing and studying biological and synthetic nano-carrier-probes for optoacoustic imaging and drug delivery. His research interests relate to the development of multifunctional nano-carriers for sensing, imaging and drug delivery. One of his aims is to develop novel nano-based tools to understand the pathobiology of disease as well as to improve disease diagnosis, drug delivery, and therapy monitoring.



Anurag Mishra

Anurag Mishra earned a master's degree in Pharmaceutical Chemistry and worked in the drug discovery team at Ranbaxy Research Laboratories (Pharmaceutical Industry) in India. Later, he won a Max Planck PhD Scholarship to carry out doctoral work at the Max Planck Institute of Biological Cybernetics under the supervision of Prof. Nikos Logothetis. After completing his PhD in 2008, he gained a Max Planck Postdoctoral Fellowship to

remain in Germany, but in 2009 he was awarded a Marie Curie Intra-European Fellowship and moved to the UK to work with Prof. David Parker. In 2013 he returned to Germany, where he is working as project lead at the Helmholtz Zentrum München to build functional chemical technology platforms (responsive imaging probes) for using multispectral optoacoustic tomography and hyperpolarized magnetic resonance imaging to study receptor processes as well as homeostasis of metals and free radicals in biological tissues. He recently received the Helmholtz ERC Recognition Award for his work.

a Institute for Biological and Medical Imaging, Helmholtz Zentrum München, Neuherberg 85764, Germany. E-mail: Vasilis.ntziachristos@helmholtz-muenchen.de ^b Chair for Biological Imaging, Technische Universität München, Munich 80333, Germany

Optical microscopy and imaging play an essential role in biological discovery, translational research or clinical diagnosis. 1-4 The advent of fluorescent imaging probes and fluorescent proteins has made optical microscopy a critical modality in the visualization and understanding of spatiotemporal dynamics of cells and proteins in vivo. 5-7 Moreover, fluorescence macroscopic imaging and tomography afforded by highly sensitive cameras have been widely applied to small-animal imaging⁸ and are increasingly considered for guiding surgery and endoscopy in the clinic.9-11 Nevertheless, due to photon scatter, the spatial resolution of optical methods falls drastically with increasing tissue depth, which limits the fluorescence visualization of fine biological details under the tissue surface. 3,12-14

Optoacoustic imaging, first introduced in the 1970s, 15 offers an alternative optical imaging method that enables high-resolution visualization as deep as several millimeters or centimeters in tissue. 16-18 The method illuminates tissue with light of transient intensity, typically nanosecond-long light pulses. Absorption of light by different tissue molecules (hemoglobin, melanin, externally administered agents) gives rise to an ultrasound wave due to thermoelastic expansion. 13,14,19,20 The ultrasound waves are then collected around the illuminated tissue and through mathematical inversion, they are converted into images of optical energy absorption in the tissue.^{3,14} There are several approaches in the literature for reconstructing the images; these include analytical algorithms like filtered backprojection (FBP), time-reversal, Fourier-based algorithms, model-based



Vasilis Ntziachristos

Vasilis Ntziachristos PhD is a Professor of Medicine and Electrical Engineering, the Director of the Chair for Biological Imaging (CBI) and of the Munich School of Bioengineering (MSB) at the Technical University of Munich and the director of the Institute Biological and Medical Imaging (IBMI) at the Helmholtz Zentrum München. He received a Diploma in Electrical Engineering Computer Science from theAristotle University

Thessaloniki, Greece, and MSc and PhD degrees in Bioengineering from the University of Pennsylvania in Philadelphia PA and served as faculty at Harvard University and the Director of the Laboratory for Bio-optics and Molecular imaging at the Massachusetts General Hospital. Professor Ntziachristos regularly serves as chair in international meetings and councils and on the editorial boards of several scientific journals and has received numerous awards and distinctions, including the Gold Medal from the Society for Molecular Imaging (2015), the Gottfried Wilhelm Leibniz prize (2013), and the Erwin Schrödinger Award (2012) and was named one of the world's top innovators by the Massachusetts Institute of Technology (MIT) Technology Review in 2004.

algorithms, and improved deconvolution algorithms. 21,22 By using ultrasound wave detection instead of photon cameras, image formation obeys the laws of ultrasound diffraction, instead of photon diffusion as in optical imaging. Therefore high-resolution optical images of tissues can be delivered, breaking through the limitations of conventional optical imaging methods. Optoacoustic imaging based on collecting ultrasound waves in the 0.1-10 MHz range achieves a resolution of $\sim 100-300$ microns through at least 3 cm of tissue in the near-infrared (NIR), since sound scattering in tissue is orders of magnitude lower than photon scattering. Even though the entire optical spectrum can be employed, light in the NIR window (650-950 nm) is attenuated less than light in the visible and IR regions; therefore NIR light is employed for small animal and human imaging applications.²³ Resolution in the range of tens of microns or better can be achieved at more superficial depths (1-10 mm), using higher frequency ultrasound detectors (10-200 MHz). This technique, termed as optoacoustic mesoscopy, also uses illumination in the visible range.

Advances in illumination technology, detectors and reconstruction methods have given optoacoustic imaging the capability of going beyond microscopic interrogation and enable highfidelity mesoscopic and macroscopic imaging.24-26 Of particular interest has been the development of fast-tuning lasers, which allow tissue illumination with multiple wavelengths within tens of milliseconds.²⁷ This advance allows real-time application of multispectral optoacoustic tomography (MSOT), a technique that illuminates tissue at multiple wavelengths and employs methods to process these images and resolve the distributions of different photo-absorbing moieties by identifying their different absorption spectral profiles^{28,29} (Fig. 1). The unmixed images in this case yield the biodistribution of reporter molecules and tissue biomarkers, imparting functional (physiological) and molecular imaging abilities. MSOT has been shown to resolve several molecular entities such as hemoglobin, melanin, myoglobin, water, lipids or a range of exogenous absorbers (dyes, nanoparticles). 13,14,28-32 Resolving the biodistribution of these molecules leads to images of vascularization, 33 tissue oxygenation and tumor hypoxia34,35 and can delineate general morphological features of tissue, including fat and water concentrations. 6,7,9-13,36 The accuracy and the sensitivity of molecular detection increases with the number of wavelengths employed: the more wavelengths used, the more molecules can be resolved and the higher the quantification accuracy achieved. 37,38 Compared with singlewavelength or two-wavelength measurements, multi-wavelength illumination and MSOT offer a more robust and sensitive approach for quantitative volumetric imaging.37,38

In addition to resolving intrinsic tissue photoabsorbers, the use of external agents (imaging probes) allows sensing a significantly richer profile of biological activity. Although common fluorochromes have absorption spectra suitable for MSOT, they do not always exhibit preferable characteristics for optoacoustic detection. Therefore probes optimized for optoacoustic signal generation are needed. MSOT imaging probes should attain high absorption cross-section (high molar extinction coefficient), low quantum yield (to maximize the nonradiative

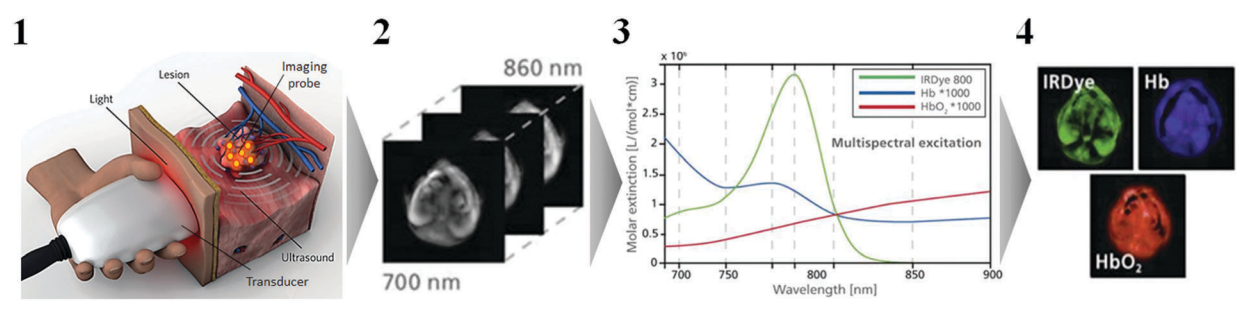


Fig. 1 Principle of MSOT. (1) A handheld optoacoustic imaging system operates similarly to an ultrasound device, except that it uses a light source to generate optoacoustic signals. (2) Optoacoustic responses are collected in the form of digital signals, after illuminating the target tissue with multiple wavelengths, and image reconstruction is performed with the acquired data. (3) Spectral unmixing algorithms identify the spectral contributions of endogenous photoabsorbing molecules in the target tissue (e.g. oxy- or deoxygenated hemoglobin), and then they separate these contributions from those due to exogenous probes (e.g. IRDye 800). (4) The result is separate images corresponding to each endogenous and exogenous chromophore. Reprinted with permission from ref. 24. Copyright 2015, Nature Publishing Group.

conversion of light energy to heat energy and produce acoustic waves) and narrow spectral profiles. The narrow spectral profile is recommended since it leads to more accurate and sensitive spectral unmixing over broad and overlapping spectral responses. Nevertheless, a prerequisite of spectral unmixing is that the different spectral profiles unmixed are sufficiently different so that they can be algorithmically separated. Probes should also be resistant to photodynamic damage or bleaching following excitation, especially for optoacoustic microscopy. A variety of imaging probes have been reported (Table 1) exhibiting absorption and photostability suitable for optoacoustic imaging. Non-specific imaging probes provide contrast wherever they are delivered. Therefore contrast enhancement relates primarily

to their biodistribution profile. Conversely, specific imaging probes, target tissue sites or moieties. In this case, contrast generation is a combination of bio-distribution and the presence of the target. Specific probes are classified into two major categories. (i) Targeted probes bind to specific cellular receptors or are preferentially encapsulated by cellular uptake mechanisms. Localized contrast enhancement is achieved through clearance of unbound probe through the renal or hepatobiliary pathways. (ii) Activatable probes change their absorption spectrum in the presence of a molecular or biochemical parameter (such as enzymes, reactive oxygen species [ROS], pH, analytes etc.). Contrast enhancement is achieved through clearance but also by means of spectral differentiation of activated vs. non-activated states.

Table 1 Overview of optoacoustic imaging probes

Probe	Туре	Size (nm)	Absorption peak (nm)	Imaging target(s)	Ref.
Green fluorescent protein (GFP)	GEC	NA	488	Drosophila Pupa	168
LacZ (produced by transgene)	GEC	NA	605-665	Tumor	171
Melanin (produced by tyrosinase transgene)	GEC	NA	680-800	Lymph nodes and tumor	172 and 177
Indocyanine Green (ICG)	NIR-FD	<2	790	Brain, lymph nodes, tumor	134, 146–148 and 193
CDnir7	NIR-FD	<2	806	Inflammation	165
IRDye800cw	NIR-FD	<2	774	Tumor	194-196
SiNc	NIR-FD	<2	770	Tumor	155
Methylene blue	NIR-FD	<2	670	Lymph nodes and tumor	159, 160 and 197
Evans blue	NIR-FD	< 2	620	Lymph nodes, brain cortical vasculature, body microvasculature	162, 198 and 199
Prussian blue	NIR-FD	<2	713	Brain	161
Polypyrrole	Pol-NS	~ 50	800	Brain and deep tissue	43 and 46
Porphysome	Pol-NS	~100	400, 680	Lymph nodes	51, 56 and 200
Conjugated polymers	Pol-NS	50-200	Depends on	Vasculature and tumor	50, 63, 71 and 74
Conjugated polymers	101115	30 200	composition	vasculature and tumor	30, 03, 71 and 74
Gold nanorods	Inorg-NP	100-1000	600-1100	Tumor and lymph nodes	76-81, 86 and 90
Gold nanostars	Inorg-NP	~100	700-800	Tumor	201–203
Gold nanoclusters	Inorg-NP	50-100	500-600	Tumor	204 and 205
Gold nanobeacons	Inorg-NP	100-200	520	Tumor and lymph nodes	206 and 207
Gold nanoprism	Inorg-NP	~100	830	Tumor	88
Gold nanoshell	Inorg-NP	100-200	600-900	Tumor	206 and 208-211
Copper sulfide	Inorg-NP	~ 20	900-1000	Tumor	116 and 117
Iron oxide	Inorg-NP	10-200	500-800	Tumor	120, 122, 123 and 212
Single-walled carbon nanotubes	Inorg-NP	5-8	600-1100	Tumor and lymph nodes	109–111 and 213
Graphene oxide	Inorg-NP	~10	500-900	Tumor	103, 104, 214 and 215
Quantum dots	Inorg-NP	5-50	630	Cells and lymph nodes	126-128 and 216

Abbreviations: GEC, genetically engineered chromophore; Pol-NS, polymeric nanostructures; Inorg-NP, inorganic nanoparticles; and NIR-FD, NIR-absorbing fluorescent dye.

Activatable probes can be further divided into irreversible probes and reversible probes depending on whether the agent undergoes a permanent or reversible structural and spectral change upon interaction with the target or in response to changes in target concentration.

In this review, we discuss the physicochemical properties as well as optoacoustic applications of several non-specific and specific imaging probes, including polymeric nanostructures, inorganic nanoparticles, organic dyes, and biological reporter genes.

1. Polymeric and inorganic optoacoustic imaging probes

1.1 Polymeric nanostructures

Polymeric nanostructures have high structural and functional flexibility, and their size, shape, and composition can be modified to optimize target specificity, optoacoustic signal characteristics, and biocompatibility. These nanostructures are well suited for optoacoustic imaging because their backbone or core can be modified to tune physicochemical properties and overall functionality.

Taruttis and colleagues reported non-invasive, specific imaging of myocardial infarction with the help of a dendritic polyglycerol sulfate (dPGS)-based NIR-absorbing specific imaging probe, which selectively targets P- and L-selectin.³⁹ The dPGS provides a highly branched, polyanionic surface that interacts specifically with P- and L-selectins via a multivalent binding mechanism. 40,41 The NIR-absorbing dye 6S-ICG propargyl was conjugated to dPGS through an aliphatic azido-linker chain. The absorption maxima of dPGS-NIR dye in phosphate-buffered saline (PBS) occur at 710 and 795 nm, whereas the fluorescence emission maximum is at 810 nm, and the quantum yield is low. These properties are favorable for detection using MSOT. In a mouse model of myocardial infarction, injecting dPGS-NIR dye followed by multi-spectral detection revealed dPGS signals in injured myocardium that increased with time from 15 min to 2 h after injection (Fig. 2(1)). These results were validated by examining tissue cryosections ex vivo. MSOT was able to image murine myocardial infarction and inflammation with spatial resolution (size or physical dimension of pixels) of ~ 200 microns at depths of several millimeters. Such performance is simply not possible using conventional optical imaging. Dendrimers offer an interesting moiety for optoacoustic imaging as they can be chemically modified to carry therapeutic or imaging agents inside or on the surface. Moreover, they have a well-defined branched structure, which can be controlled during synthesis to customize size, solubility or functional group modifications. Nevertheless, compared to other polymeric nanostructures, dendrimer synthesis requires complex synthesis steps, which can be expensive and difficult to control in large-scale production. 42 Zha and colleagues examined polypyrrole-based nanomaterials as non-specific optoacoustic imaging probes, 43 given their high absorption cross-section, efficient photothermal conversion, good photostability and excellent biocompatibility. 44-46 Nanostructures with a monodisperse, uniform size distribution of ~46 nm were

prepared via oxidative polymerization. Their size could be controlled using synthetic conditions. The molar extinction coefficient of these nanostructures at 808 nm $(2.4 \times 10^{10} \text{ M}^{-1} \text{ cm}^{-1})$ is much higher than that of hemoglobin ($\sim 1 \times 10^3 \text{ M}^{-1} \text{ cm}^{-1}$), 47,48 offering good optoacoustic signals at 808 nm at depths beyond 4 cm in chicken muscle ex vivo. 43 In vivo optoacoustic imaging of nanostructures after injection into a mouse brain has also been performed.43 Polypyrroles have a compact structure and exhibit long circulation and good biocompatibility, since no acute toxicity has been reported. Conversely, the nanostructure presents solubility and surface modification challenges. In order to enhance solubility and target specificity, Liu and colleagues reported a DSPE-PEG encapsulated conjugated polymeric structure. 49 Following a different approach to generate specific imaging probes, Balasundaram and colleagues developed folate-CP-dots, which are a functionalized folate ligand conjugated to a polymer derived from poly[9,9-bis(4-(2-ethylhexyl)phenyl)fluorenealt-co-6,7-bis(4-(hexyloxy)phenyl)-4,9-di(thiophen-2-yl)thiadiazoloquinoxaline] (PFTTQ). 50 The core and surface of these conjugated polymeric structures can be modified to tune their optical properties. The electron-donor-acceptor structure of folate-CP-dots shows a broad absorption spectrum from 700 to 850 nm. Adding functional units to the dots shifts absorption toward longer wavelengths, providing flexibility for optoacoustic imaging.

Lovell and colleagues developed non-specific imaging probes from porphysomes, which are derived from phospholipidporphyrin conjugates and which self-assemble into bilayered vesicles with a size of ~ 100 nm.⁵¹ Incorporating PEG-lipid into porphysomes improves their biodistribution. Pyropheophorbide porphysomes show absorption peaks at 400 nm and 680 nm and are highly self-quenched. Within 15 min of intradermal injection into rats, porphysomes could be visualized in the lymphatic network and draining lymph nodes (Fig. 2(2)). The hollow structure of porphysomes means they can be loaded with various drugs for cancer-specific drug delivery and photothermal therapy, or with fluorinated gas for image contrast. 52-54 The porphyrinphospholipid conjugates that make up porphysomes form microbubbles, making them well-suited for both ultrasound and optoacoustic imaging.

Huynh and colleagues described non-specific imaging probes prepared by packaging perfluorocarbon gas into a porphyrin bacteriochlorophyll-lipid shell and forming porphyrin microbubbles.⁵³ Subjecting these microbubbles to low-frequency ultrasound caused them to fragment into porphyrin nanostructures. Both the parental microbubbles and nanostructures showed an absorption peak at 824 nm. The gas encapsulated within these structures provided the ultrasound contrast, while the high density of porphyrins provided optoacoustic and fluorescence contrast. The authors injected porphyrin microbubbles into mice with KB xenografts and then applied ultrasound for 20 s to fragment the microbubbles into nanostructures. Subsequent optoacoustic imaging confirmed nanostructure formation as well as porphyrin delivery and retention in the tumor. The intrinsically multifunctional nature of porphyrins makes porphyrinbased nanostructures attractive not just for optoacoustic imaging but also for photothermal therapy,⁵⁵ theranostics

ChemComm

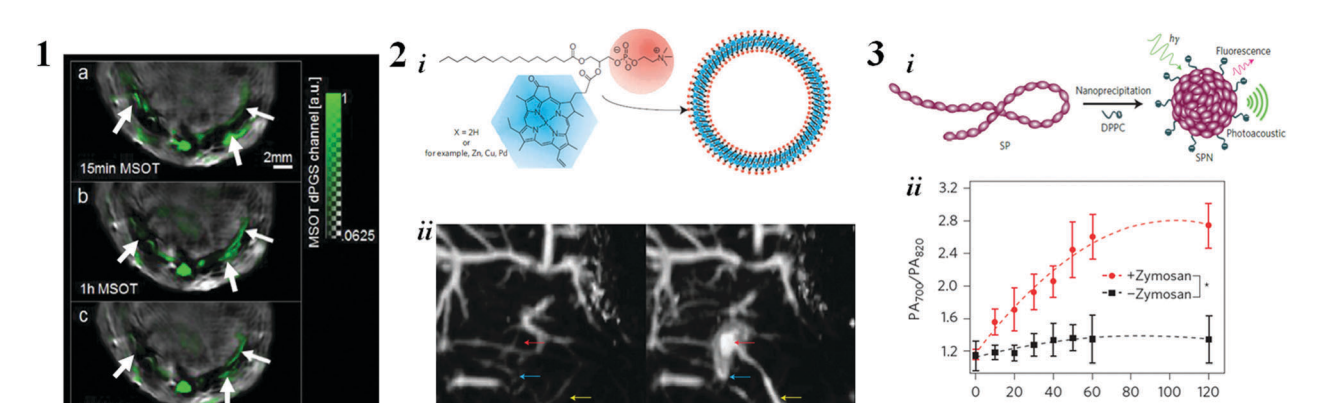


Fig. 2 Imaging polymeric nanoparticles. (1) MSOT images showing dPGS-NIR signals (green) superimposed on an image of mouse thorax illuminated at 900 nm. Images were recorded at 15 min, 1 h and 2 h after injection of dPGS-NIR dye. Arrows indicate the site of cardiac infarction in a mouse model of coronary artery ligation. Reprinted with permission from ref. 39. Copyright 2012, Elsevier Ltd. (2) Porphysome formulation and *in vivo* application are shown. (i) Schematic representation of a pyropheophorbide–lipid porphysome, showing the phospholipid head group (red) and porphyrin (blue). (ii) Rats were imaged using optoacoustic tomography before and after intradermal injection of porphysomes. Secondary lymph vessels (cyan arrow), lymph nodes (red arrow), and an inflowing lymph vessel (yellow arrow) are shown. Scale bar, 5 mm. Reprinted with permission from ref. 51. Copyright 2011, Nature Publishing Group. (3) Formulation of semiconducting polymer (SP) into nanostructures (SPN), and use *in vivo* for sensing ROS production. (ii) SPNs were prepared by nanoprecipitation. (iii) Ratio of optoacoustic amplitude at 700 nm relative to amplitude at 820 nm (PA700/PA820) at different times following injection of IR775S-conjugated SPNs in a mouse model of acute edema. *P < 0.05. Reprinted with permission from ref. 63. Copyright 2014, Nature Publishing Group.

and photodynamic therapy.⁵⁶ The origins of porphyrin in natural chlorophyll make it biodegradable and safe for *in vivo* applications.⁵⁷ Thus porphyrins have great potential for clinical translation, and nanostructures based on them may be superior to gold nanoparticles for photothermal therapy. Before commercialization and clinical translation become possible, however, simpler synthetic approaches to porphysomes are needed, as are detailed in toxicity studies.

Another class of nanostructures considered for optoacoustic imaging is based on π -conjugated semiconducting polymers, which are optically and electronically active moieties used in electronic devices, sensors, and fluorescent nanomaterials. 58-62 These polymers strongly absorb light in the NIR range, a property exploited in the development of solar cells. Pu and colleagues reported semiconducting polymer nanostructures as a new class of activatable imaging probes, 63 in which the desired optoacoustic properties are irreversibly generated after exposure to ROS. The authors focused on two semiconducting polymer derivatives based on poly (cyclopentadithiophene-alt-benzothiadiazole) (SP1) and poly (acenaphthothienopyrazine-altbenzodithiophene) (SP2) (Fig. 2(3-i)). Mixing SP1 and SP2 with 1,2-dipalmitoyl-sn-glycero-3-phosphocholine (DPPC) in one-pot, nanoprecipitation led to nanostructures of ~40 nm. Nanostructures containing SP1 produced both fluorescence and optoacoustic signals, enabling comparison of the two modalities. They further conjugated the nanostructures to an ROS-responsive derivative of cyanine dye called IR775S. The resulting nanostructures functioned as an activatable imaging probe with absorption maxima at 700, 735 and 820 nm. The peak at 700 nm reflects absorption by the semiconducting polymer, while the peaks at 735 and 820 nm reflect absorption by IR775S. The ratio of optoacoustic signals from a semiconducting polymer relative to the signal from IR775S varies directly with ROS concentration,

particularly the concentration of OONO²⁻ and ClO⁻. These ratiometric changes depend primarily on ROS-mediated oxidation of IR775S, since the signal due to the semiconducting polymer remains constant. The authors demonstrated the in vivo performance of the nanostructures by injecting them intramuscularly into mice and further administering the S. cerevisiae polysaccharide Zymosan to stimulate ROS production. The optoacoustic intensity at 820 nm was much higher in control animals than in Zymosantreated ones, indicating much higher ROS levels in treated mice (Fig. 2(3-ii)). In contrast, the optoacoustic intensity at 700 nm did not differ between the two groups of animals. Semiconducting polymer nanostructures have several advantages that make them attractive as optoacoustic contrast agents. They can be used for fluorescence, optoacoustic, and even multimodal imaging (CT, PET, SPECT). 64-66 They can also be modified into activatable optoacoustic sensors;63 and they can be used as vectors for drug and gene delivery. 67,68 They do not appear to cause systemic toxicity or biocompatibility issues. 69,70 Based on the data of Pu and colleagues, semiconducting polymeric nanostructures may have much higher molar extinction coefficients than gold nanorods or single-walled carbon nanotubes.

Time post-injection (min)

Fan and colleagues reported melanin-derived biopolymers as targeted probes in multimodal imaging. The Melanin, a natural pigment ubiquitous in human skin and several organisms, strongly absorbs light across the visible and NIR regions of the spectrum, and it can chelate metal ions (e.g. Fe³+ and $^{64}\text{Cu}^{2+}$). Fan and colleagues prepared plain, water-soluble, monodisperse melanin nanostructures with an average size of 4.5 nm, and they further enhanced water solubility and stability through PEGylation. Conjugating the resulting PEGylated nanostructures to RGD peptides rendered them selective for $\alpha_v \beta_3$ integrin, which is highly expressed in tumor neovasculature. When these RGD-conjugated PEGylated nanostructures chelated

metal ions (FeCl₃ or CuCl₂), monodisperse nanostructures with a size of 10.7 nm and neutral zeta potential formed. Injecting these monodisperse nanostructures (200 µM) intravascularly into U87MG tumor-bearing mice yielded strong optoacoustic signals 4 h later. This strong signal may reflect integrin targeting and enhanced permeability and retention (EPR) effects. Monodisperse melanin nanostructures also show potential as drug delivery vehicles, since melanin can interact via π - π interactions with drugs bearing aromatic ring structures, such as sorafenib. 74,75 Loading sorafenib into monodisperse melanin nanostructures induced their self-aggregation into particles with a size of ~ 60 nm, but this is still small enough for in vivo application. In addition, these sorafenib-loaded nanostructures generated optoacoustic signals as strong as that of an equivalent amount of monodisperse nanostructures, suggesting that these drug vehicles can serve as theranostic agents. Melanin and melanin-like agents with good optical properties, good biodegradability and chemical modifiability to enhance solubility and targetability have the potential to be translated into the clinic for multimodal imaging. Melaninbased nanostructures may be useful in diverse theranostic applications because of their ability to bind aromatic structures and drugs. Preparing these structures, however, requires polymerization, aggregation and solubility issues to be overcome.

1.2 Inorganic nanoparticles

1.2.1 Gold nanoparticles. Inorganic nanoparticles for optoacoustic contrast generation have been extensively explored. Of the several metallic nanoparticles reported so far, gold nanoparticles are particularly attractive because of their tunable properties, such as size and shape, which can alter their absorption spectrum. In addition, methods to synthesize gold nanoparticles and modify their surface are well established. Nanoparticles with other inorganic structures, such as iron and copper sulfide, have also been investigated.

Gold nanoparticles for optoacoustic imaging have been produced in a variety of shapes, including spheres, rods, shells, nanostars or triangles. Gold nanorods have attracted considerable attention as a non-specific imaging probe in vivo, drug delivery vehicle, and photothermal therapeutic agent. These nanorods exhibit a narrow absorption spectrum that can be tuned to NIR wavelengths by modifying particle characteristics such as length and diameter.76-80 The level of absorption is regulated by localized surface plasmon response. Jokerst and coworkers succeeded in controlling nanorod dimensions, which allowed them to generate different nanorod populations with absorption maxima at 661, 698, and 756 nm.81 In three cell lines, gold nanorods showed appreciable toxicity, which was significantly reduced by functionalizing the nanorods with PEG. A good optoacoustic signal was obtained from the nanorods with a resonance peak at 756 nm after injecting them intravenously into mice bearing tumor xenografts of 2008, HEY or SKOV3 cells. One limitation of gold nanorods is that, following internalization into cells, they accumulate in endosomes, such that their proximity leads to coupling of plasmon oscillations. Such plasmon coupling attenuates light absorption by the nanorods and therefore the resulting ultrasound signal.82,83 To overcome these plasmon coupling effects, Comenge and colleagues coated gold nanorods with silica, preventing them from packing closely together and reducing coupling effects.84 Experiments with nanorods coated with different silica thicknesses showed that thicker coatings led to lower packing density in endosomes, as well as stronger light absorption. When cells containing gold nanorods with a thick silica coating were implanted subcutaneously into the flank of a mouse, optoacoustic signals from the cells could be monitored for several days using MSOT. Other groups have also reported that modifying the physicochemical properties of gold nanorods (e.g. size, shape) or coating their surface to reduce coupling effects can not only improve their uptake into cells but also sharpen the absorption peaks in the spectrum.81,85

Building on gold nanorods, Lozano and colleagues combined them with NIR-dye (NIR797) labelled liposomes (NIR-liposomes) to make a nanohybrid system, 86 which formed by self-assembly driven by hydrophobic interactions. The same research group then explored the theranostic usefulness of these nanohybrids. 87 They prepared nanorod-NIR-liposomes complexed with short interfering RNA (siRNA); the overall nanohybrid was stabilized by electrostatic interactions between the cationic liposome and anionic siRNA. Injecting the nanohybrid into mice bearing 4T1 and HT29 tumors led to strong MSOT signals. This analysis indicated that the nanohybrid persisted in tumors for up to 24 h, indicating that the formulation can protect the siRNA from rapid clearance and degradation, increasing the probability of therapeutic effects. This study demonstrated not only the usefulness of gold nanorod-liposomes for delivering siRNA, but also the ability of MSOT to simultaneously resolve multiple probes, in this case, NIR-liposomes and nanorods.

In addition to gold nanorods, gold nanoparticles have been investigated as non-specific imaging probes. Bao and colleagues reported a PEGylated gold nano-prism (AuNPrs) that shows a surface plasmon resonance band in the NIR region and that produces a strong optoacoustic signal upon excitation.88 AuNPrs shows an absorption peak at 830 nm, compared to a peak at around 800 nm for gold nanorods. The spectrum of light absorbance by AuNPrs correlated well with the spectrum of the resulting optoacoustic signal. Cytotoxicity studies of AuNPrs in HT-29 cells showed the formulation to be biocompatible, and internalization of AuNPrs was confirmed using both transmission electron microscopy and two-photon microscopy. Optoacoustic imaging showed that AuNPrs injected intravenously into mice bearing HT-29 xenografts were retained in tumor tissue. In fact, the optoacoustic signal was strong enough to reveal important anatomical details about the tumor (Fig. 3(1)). Altering the size of AuNPrs can tune their surface plasmon resonance bands, potentially expanding their applications to optoacoustic imaging and photothermal therapy. Size and shape strongly influence the optical properties of gold nanoparticles in general, and synthetic methods have been reported to generate nanoparticles of various dimensions.

Liu and colleagues reported hollow plasmonic vesicles made of gold nanoparticles for non-specific biomedical imaging.89 Block copolymer-tethered gold nanoparticles self-assembled

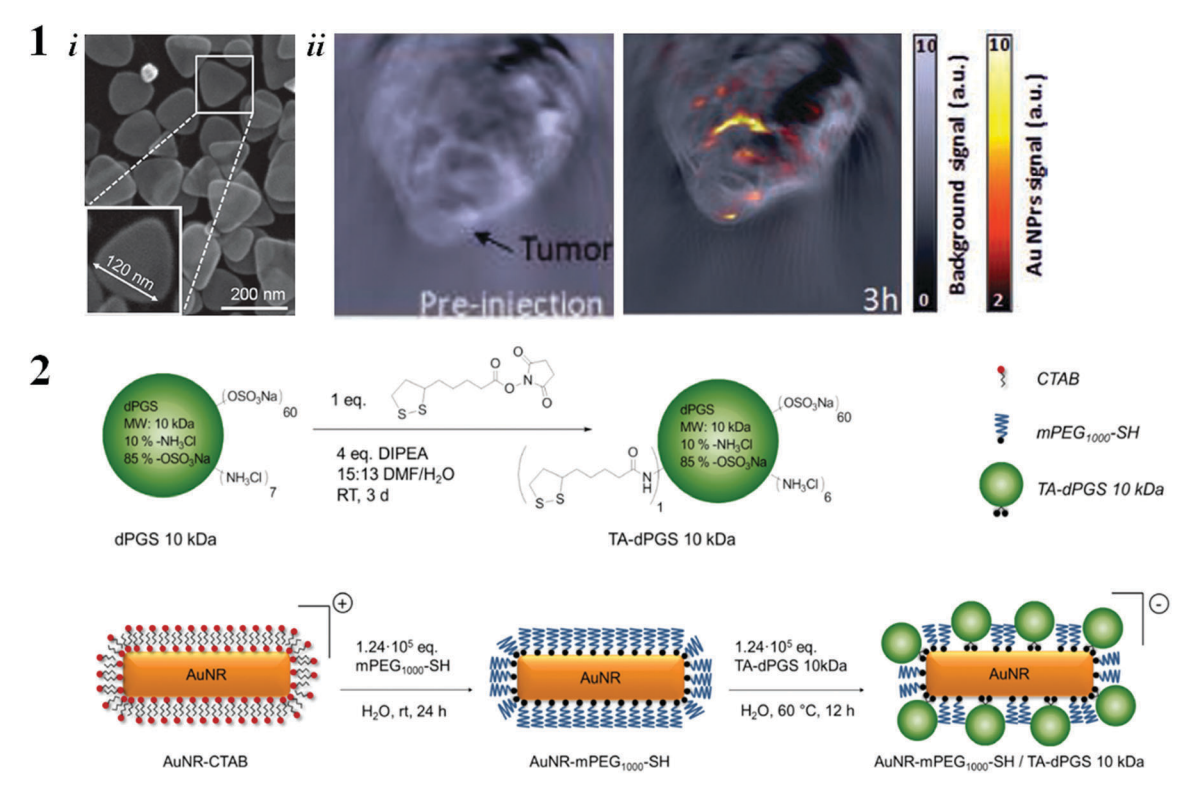


Fig. 3 (1) (i) Electron micrographs of PEGylated gold nanoprisms. (ii) Optoacoustic signals of an HT-29 tumor xenograft in a mouse prior to injection of AuNPr and at 3 h after injection. Tissue was illuminated at 710 nm. Distribution of AuNPr is shown on a red-to-yellow scale. Reprinted with permission from ref. 88. Copyright 2013, Wiley-VCH Verlag GmbH & Co. KGaA, Weinheim. (2) Preparation of gold nanorods coated with a dPGS targeting ligand. Thioctic acid-functionalized dendritic polyglycerol sulfates are synthesized, and AuNR-CTAB is functionalized with mPEG1000-SH. Next, mPEG1000-SH is partially replaced with TA-dPGS via thermally induced ligand exchange. Reprinted with permission from ref. 90. Copyright Theranostics.

into hollow vesicles, and controlling the grafting density (δ) of the block copolymer on the nanoparticle surface generated vesicles absorbing strongly in the NIR region. Monolayer chain vesicles were obtained at low δ (ca. 0.03 chains per nm²), whereas monolayer non-chain vesicles were obtained at higher δ (>0.05 chains per nm²). Chain vesicles showed stronger absorbance because of the much smaller inter-nanoparticle distance. The monolayer structure and hollow core were confirmed using transmission electron microscopy. Chain vesicles also produced nearly 8-fold higher optoacoustic signals than nonchain vesicles after subcutaneous implantation into a mouse flank. These authors demonstrated that these tethered nanoparticles could encapsulate rhodamine B, suggesting drugdelivery potential.

Several groups have explored how to convert gold nanorods into specific imaging probes, since this would allow for specific imaging as well as targeted drug delivery. Targeting strategies involve modifying the nanorod surface or conjugating nanorods to targeting ligands. To develop a targeted imaging probe, Vonnemann and colleagues attached polymeric dPGS to nanorods, 90 rendering them capable of binding with extremely high affinity to selectins, which are expressed mostly on leukocytes and inflamed endothelia.39,91 To prepare these nanorods, they were first PEGylated and then linked with TA-dPGS by ligand exchange (Fig. 3(2)). While the reaction should be thermally controlled to ensure fast, efficient ligand exchange, it is otherwise simple to perform, making it suitable for scale-up. Nanorods functionalized with dPGS bound to selectins in vitro with picomolar affinity, and they bound efficiently to K562 cells overexpressing L-selectin. In a mouse model of rheumatoid arthritis, these modified nanorods showed much higher MSOT signals in sites of inflammation than in other areas. These results illustrate the advantages of dPGS for active targeting and of PEGylation for enhancing colloidal stability. Such modification of gold nanorods may generate useful tools for imaging and photothermal therapy.

The buffer stability of gold nanoparticles and their extremely high molar extinction coefficient make them the most widely used optoacoustic imaging probes. They can be efficiently functionalized on the surface *via* thiol or PEG linkages in order to enhance biocompatibility or specificity of drug delivery or imaging. Success with gold nanoparticles depends on optimizing their shape, size and synthesis method in order to ensure the desired optical properties and biocompatibility. The potential advantages of using plasmonic gold nanoparticles for MSOT are many, including the fact that such materials can serve simultaneously as imaging probe, photothermal therapeutic, and drug delivery carrier. Their high surface-to-volume ratio means that they can absorb orders of magnitude more than small-molecule dyes. Gold nanoparticles exhibit an excellent absorption-toscattering ratio and show tunable plasmon resonance in the NIR region. Exploiting the full potential of gold nanoparticles

will require improving their photothermal stability and preventing their close packaging in cellular vesicles, where the resulting plasmon oscillations affect light absorption and signal generation, as demonstrated *in vitro* and *in vivo*. Coating the surface of gold nanoparticles with silica can reduce plasmon oscillations. ⁸⁴ It will also be important to reduce the large size of gold nanoparticles, which slows their clearance from the body and can cause toxic accumulation in the vital organs. ⁹² Therefore, it is essential to evaluate the systemic toxicity, biocompatibility and pharmacokinetics of each type of gold nanoparticle.

Feature Article

1.2.2 Carbon nanoparticles. Carbon nanoparticles are available mainly in two forms: graphene-based nanosheets and single-walled carbon nanotubes. These nanoparticles are easy to synthesize and can be tuned to absorb in the NIR range; they can also be functionalized with diverse entities, such as small-molecule dyes, drugs, polymers and targeting ligands. This makes carbon nanoparticles suitable for diverse applications, including as biosensors, scaffolds for tissue engineering, nanocarriers for drug and gene delivery, and anti-cancer phototherapeutic agents. ⁹³

1.2.2.1 Graphene. Graphene is an allotrope of carbon atoms in the form of a hexagonal 2D (honeycomb) lattice. It possesses electronic properties of a zero-gap semiconductor, because its conduction and valence bands meet at the Dirac points, generating a broad absorption spectrum in the NIR region. Graphene is quite efficient at photothermal conversion, and its large surface area can be loaded with drugs as well as functionalized for greater biocompatibility or tissue targeting.94-96 Several strategies have been developed to produce graphene sheets from graphite, most of which rely on chemical oxidation of graphite to produce heavily oxidized graphene oxide sheets. However, these methods usually result in layered, defect-ridden structures. Thus it is difficult to obtain high-quality graphene on a large scale. Several approaches have been proposed to obtain more uniform graphene sheets, including chemical vapor deposition, microwave-assisted synthesis or use of nano-sized starting materials such as graphite nanofibers or carbon fibers. 97-102

Patel and colleagues fabricated graphene sheets using microwave-assisted nitronium oxidation chemistry. 103 By increasing the concentration of NO₂⁺, they obtained a high concentration of graphene nanosheets that showed strong absorption in the NIR range and generated strong optoacoustic signals. The absorption coefficient of these nanosheets at 808 nm is 22.7 L g⁻¹ cm⁻¹, substantially higher than that of indocyanine green (ICG, 13.9 L g⁻¹ cm⁻¹). The non-luminescent nature of these nanosheets means that most of the absorbed optical energy is transformed to heat, explaining the strong optoacoustic signals observed. In contrast, conventional graphene oxide nanosheets do not show detectable optoacoustic signals after illumination at 700 or 800 nm. In another approach to develop graphene as a non-specific imaging probe, Yang and colleagues reported reduced graphene oxide nanosheets to which iron oxide nanoparticles were anchored for use in optoacoustic imaging. 104 Functionalizing this nanocomposite with polyethylene glycol enhanced biocompatibility and stability. The resulting material shows strong absorbance in the NIR range and strong magnetic properties, allowing its use in multimodal imaging-guided photothermal therapy. Injecting the material into mice bearing 4T1 tumors led to high uptake into tumors, based on optoacoustic tomography and magnetic resonance imaging.

1.2.2.2 Carbon nanotubes. Most studies of carbon nanoparticles as optical probes have focused on single-walled carbon nanotubes (SWNTs), which are nanocylinders of graphene sheets wrapped up to form a tube of diameter \sim 1-2 nm. Their optical properties can be tuned by changing tube diameter and chirality, or by introducing surface modifications. 105-108 SWNTs have been used in fluorescence imaging, Raman detection, and optoacoustic imaging. De la Zerda and colleagues demonstrated that SWNTs could be used as a targeted optoacoustic imaging probe. 109 To target the probe to tumors, they conjugated it to cyclic RGD peptides via a polyethylene glycol-5000 phospholipid (PL-PEG5000). These modified SWNTs gave maximal optoacoustic signals after illumination at 690 nm, where the ratio of optoacoustic signals from SWNTs relative to that from hemoglobin was also the greatest. In mice bearing U87MG tumor xenografts, SWNT-RGD accumulated in the tumor (Fig. 4(1)), which showed 8-fold higher optoacoustic signals than tumors containing unmodified SWNTs. These optoacoustic results were confirmed using Raman microscopy. In another study, De la Zerda and colleagues enhanced RGD-conjugated SWNTs by conjugating them to the dye ICG. 110 The resulting nanoparticles showed peak absorbance at 780 nm, where the absorbance was 20-fold higher than with plain SWNTs. Optoacoustic signals from U87MG tumor xenografts was much higher using ICG- and RGD-conjugated SWNTs than using negative-control SWNTs conjugated to ICG and a different peptide. These experiments showed that ICG labeling of RGD-SWNTs does not interfere with their ability to bind molecular targets with sub-nanomolar affinity or to provide high optoacoustic contrast. In an analogous approach, researchers have reported other nanohybrids for targeted optoacoustic imaging and photothermal therapy, such as gold-plated carbon nanotubes.111 These nanotubes are conjugated to an anti-LYVE-1 antibody, which binds to lymphatic endothelial hyaluronan receptor-1. Such antibodyfunctionalized, gold-plated nanotubes combine targeting specificity with dual plasmonic behavior.

High photostability, high molar extinction coefficient and easy functionalization of carbon nanoparticles give them advantages over many gold nanoparticle optoacoustic imaging probes. Carbon nanoparticles can be used for multi-modal imaging, including Raman, optical and optoacoustic imaging, and their electronic and optical properties can be customized by attaching different polymers. Their unique hollow geometry can easily accommodate guest materials such as metal nanoparticles, which allows the advantages of both materials to be combined. Carbon nanoparticles are also more dispersible and therefore more biocompatible than gold in most biological systems. On the other hand, carbon nanoparticles show several of the same disadvantages as gold nanoparticles (see Section 1.2.1). Various synthetic strategies have been described to modify the

ChemComm

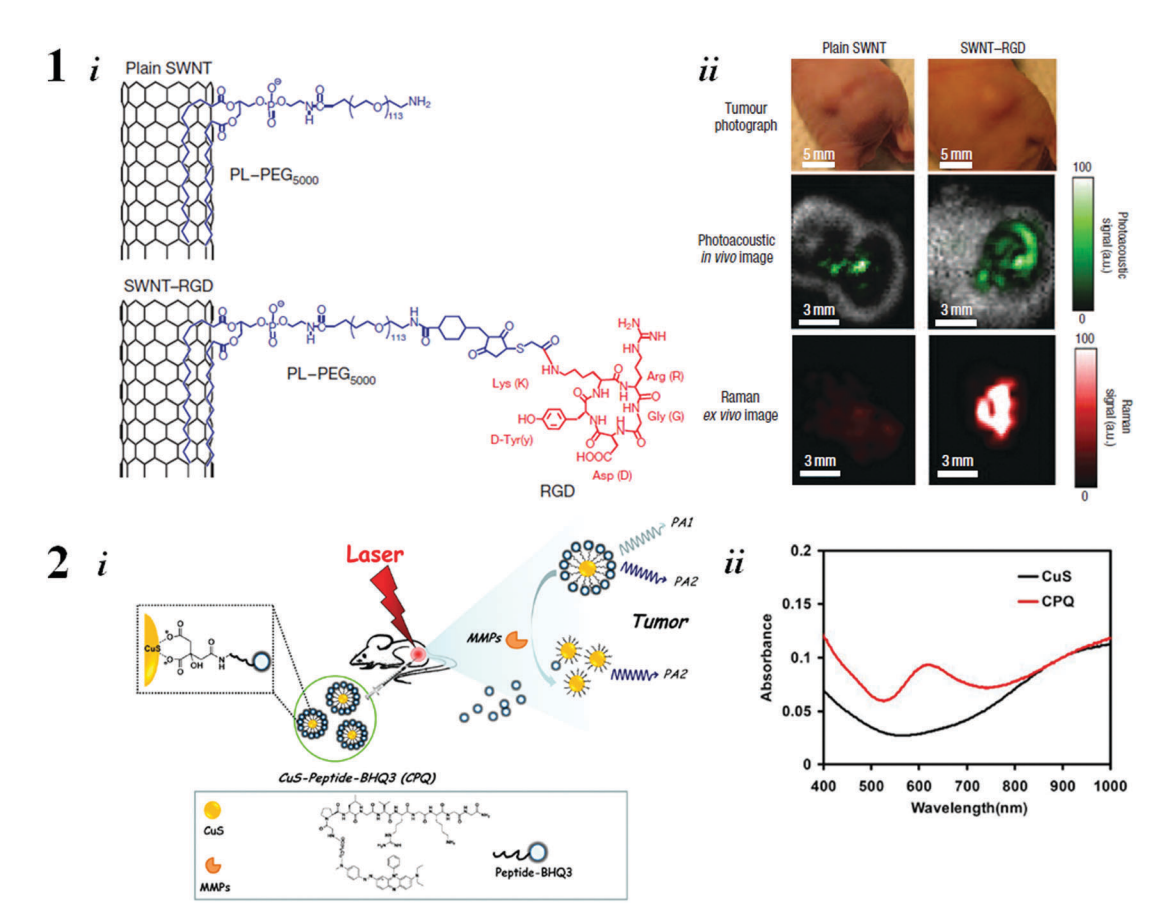


Fig. 4 (1) (i) Schematic illustration of plain single-walled carbon nanotubes (plain SWNTs) and SWNTs conjugated to the targeting peptide RGD (SWNT-RGD). Phospholipid binds to the SWNTs, connecting the PEG₅₀₀₀ and RGD to the nanotubes. (ii) Photographs of tumor-bearing mice and the corresponding optoacoustic subtraction images (green) after injection with plain SWNTs or SWNT-RGD. These results were validated by excising tumors and scanning them using Raman microscopy (red). Reprinted with permission from ref. 109. Copyright 2008, Nature Publishing Group. (2) (i) Schematic illustration of the MMP-activatable CPQ nanoprobe, in which BHQ3 is conjugated to CuS nanoparticles via an MMP-cleavable peptide linker. (ii) UV-vis-NIR spectra of CuS and CPQ nanoparticles. Reprinted with permission from ref. 112. Copyright Theranostics.

surface, size and shape of carbon nanoparticles to enhance biocompatibility and targeting ability. In some cases, surface modifications have been reported to substantially reduce potential toxicity.

1.2.3 Copper sulfide. Copper sulfide (CuS) absorbs light at wavelengths in the far-NIR region, and citrate-coated CuS is highly stable in physiological solutions. Yang and coworkers reported an activatable probe that consists of CuS and black hole quencher 3 (BHQ3) and that is irreversibly activated by matrix metalloproteinases (MMPs) (Fig. 4(2)).112,113 They covalently conjugated CuS to BHQ3 via an MMP-sensitive linker. The CuS nanoparticles exhibit a high absorbance band at ~930 nm, and conjugation with BHQ3 generated another broad peak between 600 and 700 nm. In the tumor microenvironment, abundant MMPs can cleave the MMP-sensitive linker, 114,115 releasing the BHQ3. The BHQ3 is then cleared from the tumor, while CuS remains behind. As a result, the ratio of optoacoustic signals at 680 nm relative to signals at 930 nm decreases, as the authors demonstrated in an in vivo tumor model. Furthermore, researchers demonstrated the usefulness of CuS nanoparticles not only for optoacoustic imaging but also for photothermal therapy and drug delivery. 116,117

Zha and colleagues reported CuS nanoparticles stabilized using gelatin-conjugated doxorubicin as a multipurpose platform for use in optoacoustic imaging, enzyme-responsive drug release, and photothermal therapy.117 Gelatin, a natural macromolecule digested by gelatinase in tumor tissue, has also been used to prepare stable nanoparticles such as Fe₃O₄ and CdTe quantum dots. 118 In vivo experiments showed that CuS nanoparticles with gelatin-conjugated doxorubicin could work well as optoacoustic imaging probes to identify cancerous lesions. They can also kill tumor cells effectively by combining the effects of photothermal therapy and chemotherapy. 117

The limited data available so far on copper sulfide particles for optoacoustic imaging suggest that their principal advantages are that they can be used in the far-NIR region to increase SNR, they are easy to synthesize and have tunable absorption peaks, and they can be combined with other agents for multimodal imaging involving, for example, positron emission tomography and magnetic resonance imaging. However the in vivo toxicity of copper is not well established, which is crucial for clinical applications.

1.2.4 Iron oxide nanoparticles. Superparamagnetic iron oxide nanoparticles (SPIONs) are FDA-approved nanoprobes used mainly in magnetic resonance imaging. Their biocompatibility

and optical stability also make them useful as specific, nonactivatable optoacoustic imaging probes.¹¹⁹ Xi and colleagues described iron oxide nanoparticles labeled with an NIR-absorbing dye and conjugated to amino-terminal fragments of urokinase plasminogen activator (uPA), allowing targeted imaging of tissue containing the uPA receptor. 120 This receptor is highly expressed in various cancers, including breast cancer. 121 The authors injected their dve-labeled uPA-nanoparticle conjugate into tumor-bearing mice, and measured the optoacoustic signal at wavelengths from 730 nm to 870 nm. The conjugate showed stronger absorption at 730 nm than at 800 nm or 850 nm. It generated an optoacoustic signal 3-fold greater than that of conjugates in which the uPA targeting moiety was replaced with bovine serum albumin, and 10-fold greater than that of non-injection controls.

Yu and colleagues reported nanocomposites based on ultrasmall Fe₃O₄ nanoparticles as magnetically targeted theranostic agents. 122 These nanocomposites were prepared by conjugating Fe₃O₄ nanoparticles to the surface of MoS₂ nanoflakes, which were then modified with poly-(ethylene glycol) to improve biocompatibility. MoS2 nanoflakes exhibit a photothermal effect under irradiation with an 808 nm laser, and the Fe₃O₄ nanoparticles ensure magnetic targeting. Under the influence of an external, localized magnetic field, superparamagnetic Fe₃O₄ accumulates in the tumor, enabling tumor-specific delivery of therapeutic agents and reducing toxic effects in healthy tissue. The authors demonstrated the usefulness of these nanocomposites in vitro and in vivo for magnetically targeted imaging via magnetic resonance and optoacoustics. Similarly, Yu and coworkers reported magnetic Hägg iron carbide (Fe5C2) nanoparticles as multifunctional probes for magnetic resonance imaging, photothermal therapy, and optoacoustic tomography for imaging-guided therapy. 123 These nanoparticles are small, stable, and biocompatible, and they show high magnetization and NIR absorbance, making them potentially well-suited for imaging-guided cancer therapy.

Iron oxide nanoparticles, already clinically approved by the US Food and Drug Administration (FDA), are widely used for magnetic resonance imaging. Thus, iron oxide-based MSOT probes may be closer to clinical implementation than other types of probes. SPIONs allow multimodal imaging and multifunctional applications. They have higher molar relaxivities, so they may be useful at low concentrations as blood-pool and tissue-specific agents. Their biocompatibility can be improved easily by coating with dextran or silica. 124,125

1.2.5 Quantum dots. Quantum dots (QDs) were primarily developed as fluorescent probes for non-invasive in vivo imaging of tumors, lymph nodes, vascular networks and cellular trafficking. 126 It turns out that they can also generate strong optoacoustic signals by virtue of their limited quantum yields (20-40%), broad absorption spectra (from 400 to 750 nm), and conversion of absorbed light energy to heat via non-radiative relaxation pathways. 127 Shashkov and colleagues demonstrated that quantum dots excited with nanosecond-pulse lasers could be used as non-specific probes in optoacoustic and photothermal microscopy (420–900 nm). 128 Quantum dots, in particular, show potential for tracking tumors and lymph nodes via

fluorescent and optoacoustic imaging, as well as for photothermal therapy. 126-128

Similar to other inorganic nanoparticles, QDs offer excellent photostability and narrow, tunable absorption and emission bands. Their high molar extinction coefficient and high quantum yield make them useful for dual-mode optical and optoacoustic imaging. However, the efficiency with which QDs convert laser energy to acoustic emission must be optimized in order to exploit their full potential for MSOT. The inorganic composition of QDs makes them more stable and resistant to photobleaching than organic dyes, 129 as well as more resistant to metabolic degradation in vivo, which can contribute to cytotoxic effects. The cytotoxicity of QDs is a major obstacle to their clinical translation. They accumulate in the kidney, spleen, and liver, 130 but few details are known about how QDs are metabolized, degraded and cleared in the body.

Overall, polymeric and inorganic imaging probes have shown tremendous promise as effective imaging probes because of their ability to provide good contrast as well as strong signal density and signal amplification. They also allow integration of multiple functionalities into a single probe, and they can provide a large surface area for carrying different agents, including drugs. On the other hand, their large size means that these probes penetrate tissue less efficiently than small-molecule probes (see next section), and they can elicit immune responses. Many of these particles are either non-degradable or tend to aggregate in biological fluids. Therefore, applying these set of probes to imaging in the clinic will require further work to reduce their toxicity and immunogenicity, as well as increase their biocompatibility. Studies should investigate their biodegradation and aggregation tendency along with their biocompatibility or systemic toxicity. Studies should also measure their specificity, sensitivity and in vivo kinetics and dynamics.

2. Small-molecule organic dyes

Small-molecule organic dyes have also been studied for optoacoustic signal generation and contrast modulation. 13,14,131 The chemical structure of probes can be tuned to optimize their physicochemical properties, such as solubility, molar extinction coefficient and photo-bleaching; these properties can be optimized, respectively, by introducing hydrophilic groups, triplet state quenchers and stabilizing groups. The optoacoustic signal enhancement of small molecules can be achieved by having a series of π -bonds and aromatic ring structures that allow high photon absorption with minimal radiative decay (quantum yield) of the probes. The spectral range of chemical dyes can be modified by attaching electron-donating or electron-withdrawing groups at different positions on the dyes. Dyes may also be transformed with targeting ligands or encapsulated into nanocarriers to enhance half-life and optoacoustic signals. 131-136

Cyanine dyes, which consist of aromatic nitrogen-containing heterocycles linked *via* polymethine chains, ^{131,137,138} are among the most widely used dyes in optoacoustic imaging. ICG is an FDA-approved, non-specific zwitterionic heptamethine cyanine

dye widely used to provide static contrast in both fluorescence and optoacoustic imaging. 138-140 It is used mainly to examine cardiac and hepatic function, hepatic blood flow, and ophthalmic angiography, as well as to identify sentinel lymph nodes. 141-144 In aqueous solution, ICG shows an absorption maximum at 780 nm, a molar extinction coefficient of 1.2 \times 10⁵ M⁻¹ cm⁻¹ and a fluorescence quantum yield <1%. In serum, the quantum yield can rise to as high as 12%.145

Kim and colleagues reported the use of ICG to map sentinel lymph nodes and lymphatic vessels in rats. 146 They performed volumetric optoacoustic and planar fluorescence imaging before and after intradermal injection of the dye (1 nmol L^{-1}). The strong contrast provided by the dye allowed clear visualization of lymphatic networks and sentinel lymph nodes at different depths, raising the possibility that ICG can be used for mapping sentinel lymph nodes and evaluating tumor metastasis. However, ICG in these initial studies showed a half-life in vivo of only 3-4 min, relatively low photostability and high binding to plasma proteins, suggesting the need to deliver the dye in a nano-encapsulated form. Beziere and colleagues engineered liposomal-ICG (LipoICG) by taking clinically approved PEGylated liposomes (formulated for Doxil), and incorporating ICG into the lipid bilayer. 147 Liposome-embedded ICG absorbed light much more strongly than free ICG did, at least under these in vitro conditions, and it showed significantly higher optoacoustic signals. Using MSOT, the authors reported that LipoICG showed good optoacoustic signals up to 24 h after injection into mice bearing 4T1 or HT29 tumors (Fig. 5(1)). Free ICG, in contrast, underwent rapid renal clearance. The tumor signal gradually increased after injection, peaking at 4 h and remaining constant thereafter. These results demonstrate the excellent potential of liposome-embedded ICG for optoacoustic imaging in the clinic. Coupling this liposome-ICG approach with the targeting efficiency of antibodies, Lozano and co-workers functionalized liposomal-ICG with an anti-MUC-1 humanized monoclonal antibody (hCTM0.1).148 In mice bearing 4T1 or HT29 tumors, MSOT showed that antibody-targeted liposome-ICG accumulated in tumors faster and to a greater extent than did non-targeted liposomal-ICG. The authors extended the clinical potential of this system by loading it with doxorubicin, opening the door to imaging-guided cancer therapy.

To overcome the photophysical challenges of heptacyanine dyes, researchers have modified the polymethine linkers with cyclohexenyl substitutions, substantially improving the molar extinction coefficient and photostability. 149,150 Onoe and colleagues reported that these non-specific probes can be stabilized by irradiating them several times with a laser. 150 They introduced a triplet state quencher moiety into the symmetrical cyanine dye to quench ¹O₂ generation and prevent degradation of the probe due to singlet oxygen. They observed that the modified cyanine derivatives emit strong optoacoustic signals and show good photostability against multiple irradiations. Others have shown that substitution with electrondonating groups can improve photostability, 134 while introduction of carboxylic or sulfonic acid groups can enhance solubility. 135,136 Further work is needed to improve the cyanine structure and accelerate its development for imaging in the clinic.

Aiming to bring functional molecular optoacoustic imaging to the brain, Sim and colleagues developed two targeted, reversibly activatable probes (L¹ and L²) based on cyclic heptacyanine dyes and conjugated to competitive and non-competitive antagonists of glutamate (Fig. 5(2)). 151 These probes bind selectively to N-methyl-p-aspartate (NMDA) receptors on the neuronal surface,

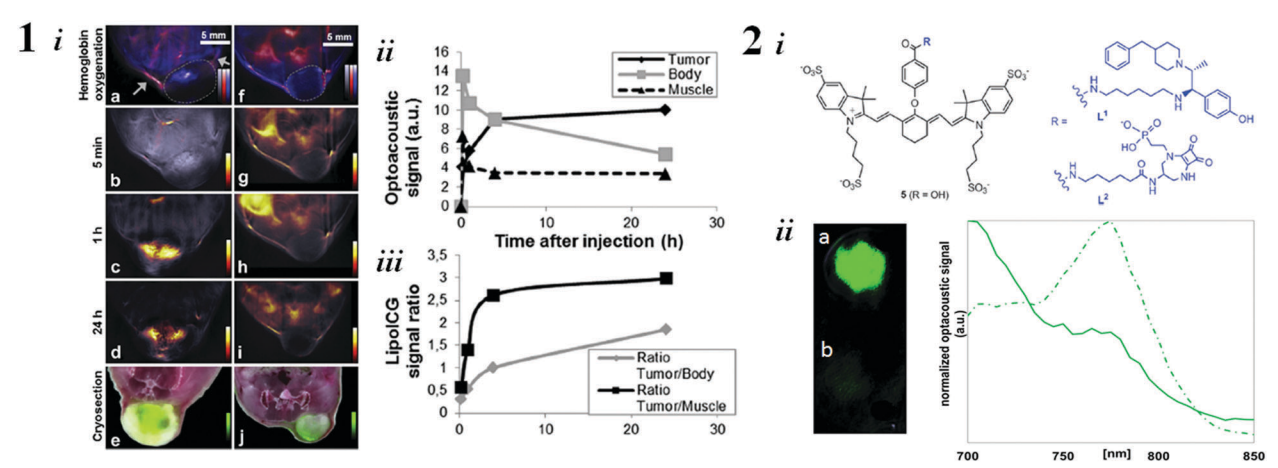


Fig. 5 (1) Kinetics of accumulation of liposomal-ICG in mouse tumor models imaged with MSOT. (i) MSOT images of a 4T1 tumor (a-d) or HT29 tumor (f-i) before injection of the liposomal formulation and at different time points after injection. Tissue was illuminated at 800 nm. The corresponding cryosections are shown in panels e and j. (ii) Optoacoustic signal intensity due to the liposomal formulation in the tumor (black line), in the entire body without the tumor (gray line) and in the back muscles (dashed line). (iii) Ratio of optoacoustic signal intensity in the tumor relative to signal intensity in the entire body without tumor (gray line) or to signal intensity in the back muscles (black line). Reprinted with permission from ref. 147. Copyright 2014, Elsevier Ltd. (2) (i) Optoacoustic imaging probes for tagging of the NMDA receptor. (ii) (Left panel) Optoacoustic signal of differentiated NSC-34 cells following treatment with heptacyanine dye-based L^{1} (20 μ M, 30 min) alone (upper image), or following treatment with probe and then two washes with 1 mM glutamate (lower image). The optoacoustic signal of the probe was strongly reduced in the presence of glutamate. (Right panel) Comparison of optoacoustic signals between probe L¹ bound to NSC-34 cells (solid line) and free probe L¹ in solution (dot-dash line). Reprinted with permission from ref. 151. Copyright The Royal Society of Chemistry (RSC).

allowing optoacoustic imaging. Both probes show broad absorption bands centered at 776 nm and extinction coefficients of $2.4 \times 10^5 \text{ M}^{-1} \text{ cm}^{-1}$. Conjugating the probes to glutamate antagonists prevents their receptor-mediated endocytosis, 152 while the negatively charged sulfonate group in the heptamethine cyanine core reduces nonspecific protein binding.¹⁵³ The authors confirmed that one of the probes binds specifically to the NMDA receptor in NSC-34 differentiated neurons and that its absorption at 700 nm is significantly higher than that of the un-bound probe. The probe binds deep within the NMDAR cleft, where the cavity creates a more hydrophobic environment than bulk solvent, shifting the absorption maximum by 80 nm. These authors injected the same probe intracranially into the mouse motor cortex and were able to visualize it deep inside the tissue using MSOT. These results lay the foundation for further development of probes that allow in vivo, non-invasive optoacoustic imaging of the NMDA receptor and of dynamic changes in glutamate concentration. Another specific, reversibly activatable probe for dynamic sensing of calcium has been engineered by Mishra and colleagues. They reported the first reversible heptacyanine-based Ca²⁺ sensing probe that operates in the near-NIR region for optoacoustic imaging (Fig. 6(1)). 154 The

probe absorbs light in the NIR range with a high molar extinction coefficient (1.9 \times 10⁵ M⁻¹ cm⁻¹ in buffer), and it shows high photobleaching resistance. These properties make it ideal for optoacoustic imaging. In the presence of Ca²⁺, the probe absorbance at 765 nm is halved, causing a substantial decrease in optoacoustic signals; this change is reversed upon addition of EDTA. The substantial reduction in excitation and emission wavelengths upon Ca²⁺ coordination can be explained by transfer of a lone pair of electrons from the N atom in APTRA-morpholinoamide (donor) to IR-780 (acceptor). The probe shows selectivity for Ca²⁺ over other biological cations $(K_{DCa} = 11.3 \mu M)$. Therefore, heptamethine cyanine may be a useful scaffold for generating a series of cation-specific probes that absorb in the NIR range for real-time molecular monitoring deep in tissues using MSOT.

Beziere and colleagues reported a new class of non-specific imaging probes based on silicon 2,3-naphthalocyanine bi(trihexylsilyloxide) (SiNc, Fig. 6(2)), which may be suitable for theranostics. These dyes can generate stable optoacoustic signals as well as trigger ROS production.155 The optical and optoacoustic spectra of SiNc correlate at wavelengths longer than 770 nm, while the optoacoustic signal is greater than the

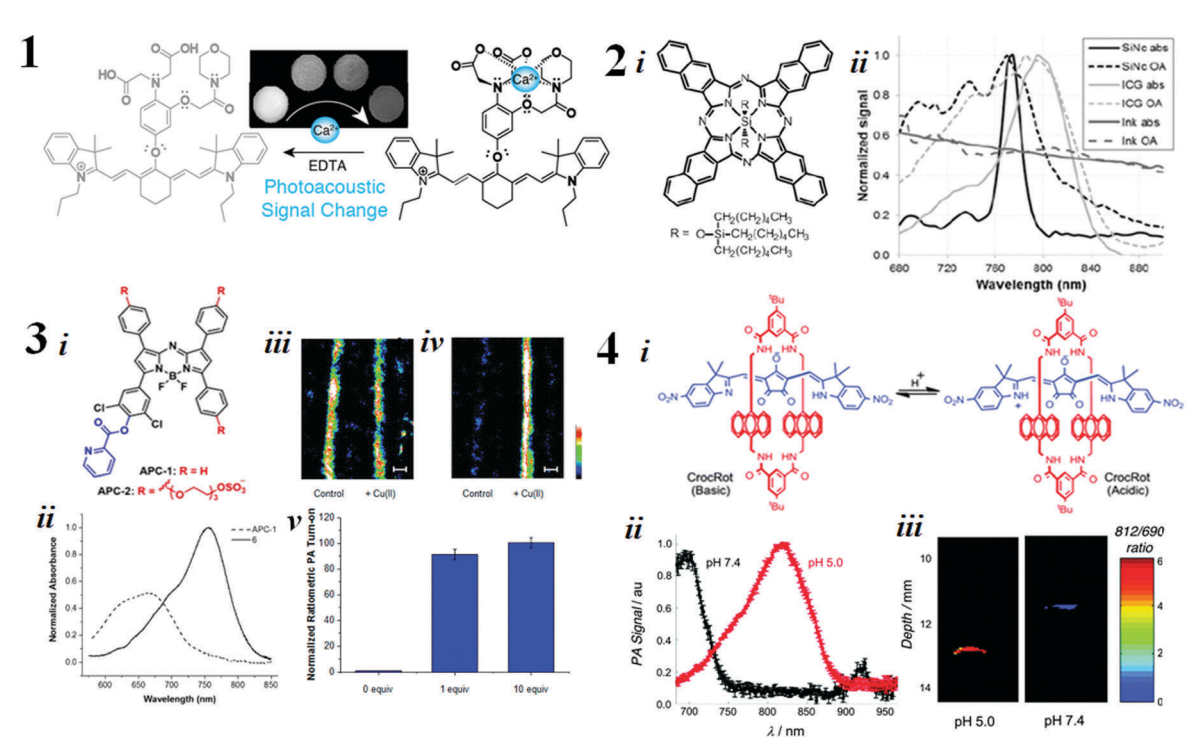


Fig. 6 (1) Reversible NIR calcium (Ca^{2+}) sensing photoacoustic probe (L) in unbound and Ca^{2+} -bound forms. Reprinted with permission from ref. 154. Copyright 2016, American Chemical Society. (2) (i) Structure of SiNc. (ii) Comparison of light absorption and optoacoustic signals from SiNc, ICG and Ink is shown. Reprinted with permission from ref. 155. Copyright 2015, The Society of Nuclear Medicine and Molecular Imaging, Inc. (3) (i) Chemical structures of metal-detecting probes APC-1 and APC-2. (ii) Normalized absorbance spectra of APC-1 (2 µM, dashed line) and its hydrolysis product 6 (2 μM, solid line) in PBS containing 0.1% CrEL (pH 7.4). (iii and iv) Optoacoustic images of 10 μM APC-2 (PBS + 0.1% CrEL, pH 7.4) in FEP tubing overlaid with phantom (1 cm thick) treated with 0 or 10 equivalents of Cu(ii) and excited at (iii) 697 or (iv) 767 nm. Pseudo-coloring indicates intensity from the highest (white) to lowest (black). Scale bar, 2 mm. (v) Quantification of APC-2 treated with 0, 1, or 10 equivalents of Cu(II) for 90 min. Blue bars indicate normalized ratiometric turn-on responses calculated from the ratio of optoacoustic signals at 767 nm to signals at 697 nm. Reprinted with permission from ref. 157. Copyright 2015, American Chemical Society. (4) (i) The pH-sensitive interconversion between basic and acidic forms of croconaine rotaxane (CrocRot). (ii) Optoacoustic scans of CrocRot at pH 7.4 (black) and pH 5.0 (red). (iii) Ratiometric photoacoustic images of two phantoms containing CrocRot at pH 7.4 or 5.0 at a depth of 11-13 mm in light-scattering medium. Reprinted with permission from ref. 158. Copyright The Royal Society of Chemistry (RSC).

optical one at shorter wavelengths. The sharp absorption band of SiNc around 770 nm makes it well-suited to optoacoustic studies, since light at these wavelengths can penetrate several centimeters into tissues. Light absorption by SiNc between 770 and 800 nm falls off much more steeply than that of ICG, giving SiNc an advantage for optoacoustic imaging. In MSOT experiments, the authors found that SiNc photobleached less than ICG and showed a ≈4-fold higher molar extinction coefficient (5.0 \times 10⁵ M⁻¹ cm⁻¹). Pulsing SiNc at an energy of 15 mJ per pulse did not lead to loss of optoacoustic signals after 1 h, although energies of 40 or 80 mJ per pulse reduced the signal by up to 70%. Even so, photobleaching of SiNc at 80 mJ was slower than that of an ICG emulsion. The optoacoustic signal per mole of SiNc was nearly 2-fold higher than that of ICG, with the two dyes giving comparable signal strength after 1 h of illumination. The feasibility of using SiNc for optoacoustic imaging was confirmed in studies of mice bearing HT29 tumors. SiNc dyes containing polycyclic phthalocyanines offer the potential of triggering ROS generation following activation with high-energy light. This opens the door to possible application as a theranostic agent or photodynamic therapy.

Levi and colleagues developed irreversibly activatable optoacoustic probes for detecting the activity of specific enzymes. 113 The idea is that the target enzyme modifies the probe, which is then internalized into cells, where it can accumulate and be imaged. The authors tested this idea using an activatable cellpenetrating peptide (ACPP) that can be cleaved by MMP-2, which is expressed mainly in cancers. They conjugated the ACPP to chromophores BHQ3 and Alexa750, which generate similarly strong optoacoustic signals at respective wavelengths of 675 and 750 nm. Since BHQ3 was conjugated to the part of the probe taken up by cells, MMP-2-mediated cleavage led to optoacoustic signals at 675 nm. In a different strategy to generate an irreversibly activatable probe, Dragulescu-Andrasi and colleagues developed an enzyme-sensitive probe that targets furin via a short peptide (arginine-valine-valine-arginine), which acts as a furin substrate and which is conjugated to the fluorophore Atto740 consisting of cysteine-lysine-(cyano-6amino-benzothiazole). 156 Cleavage of the peptide bond between cysteine and lysine causes the cyano-6-amino-benzothiazole moiety to undergo a bioorthogonal condensation reaction, and the reaction product aggregates into nanostructures at the target site. Studies in vitro and in vivo in mice bearing MDA-MB-231 tumors showed that the optoacoustic signal from the probe was much higher when the tumors expressed furin than when they did not. Such probes may allow in vivo monitoring of enzyme activity. In a third approach to generating irreversibly activatable probes, Li and colleagues reported probes APC-1 and APC-2 for metal detection based on an aza-BODIPY scaffold.¹⁵⁷ Cu²⁺ activates 2-picolinic ester bond cleavage in these probes, irreversibly altering the absorption spectrum as well as the optoacoustic signal (Fig. 6(3)). Such chemoselective visualization of Cu2+ may be useful for studying chronic neurological disorders such as Alzheimer's disease.

Demonstrating the power of reversibly activatable imaging probes, Guha and colleagues reported croconaine dyes that

show strong absorption in the NIR range and can switch in a pH-dependent way between an anionic basic form and a zwitterionic acidic form, resulting in changes in the absorption spectrum and therefore optoacoustic signals (Fig. 6(4)). 158 The dye also shows pH-dependent photothermal heating. To prevent electronic coupling, the authors entrapped the croconaine dye in a tetralactam macrocycle, generating croconaine rotaxane, which they then formulated into stealth liposomes. The optoacoustic signal intensity of croconaine rotaxane is comparable to that of ICG.

Song and colleagues reported that methylene blue, another FDA-approved synthetic dye widely used for biological staining, can serve as a non-specific probe in optoacoustic imaging. 159 The hydrophilic dye shows an absorption peak at 670 nm. Injection of a 1% solution of the dye into the forepaw pad of a rat allowed imaging of sentinel lymph nodes with good contrast shortly after injection. While this contrast gradually decreased for surrounding vessels, it remained for the sentinel lymph nodes. It is possible that even higher optoacoustic signal or deeper imaging could be achieved with higher laser fluence, since the fluence in these experiments was 5-fold lower than the maximum permissible exposure. Combining methylene blue with microbubbles can allow both ultrasound and optoacoustic imaging. 160 Other organic dyes showing high absorption in the NIR region have also been explored as optoacoustic imaging probes, including Evans blue (620 nm), Coomassie blue (595 nm) and Prussian blue (700 nm). 161-164 Most of these dyes undergo rapid renal clearance or photobleaching, limiting their in vivo suitability.

In contrast to the standard targeting approach of conjugating probes to antibodies, peptides or oligonucleotides, Kang and colleagues generated and screened structurally different, photostable, NIR-absorbing dyes for their ability to act as specific, non-activatable imaging probes. 165 They found that the CDnir7 probe could selectively detect macrophages and visualize inflammation or tumors in vivo. The macrophage specificity of the CDnir7 probe was observed during both cell-based screening and in an in vivo model of lipopolysaccharideinduced inflammation. The authors tested the accumulation of CDnir7 in mice bearing orthotopic 4T1 breast tumors, which are known to recruit large numbers of tumor-associated macrophages.¹⁶⁶ CDnir7 accumulated rapidly in the tumor, reaching maximal levels within 10 min and remaining detectable beyond 3 h. The ability of CDnir7 to target inflammation in vivo was confirmed using IVIS and FMT imaging.

Creating and screening libraries of synthetic small molecules is an important way to identify probes that respond to specific targets. This approach has already led to several functionalized dyes with backbones absorbing in the NIR range suitable for optoacoustic imaging. Such dyes include cyanine, BODIPY, porphyrin, croconaine, AlexaFluor740, Atto740, and squaraine. 167 This functionalization has produced organic dyes that can measure, non-invasively and dynamically, changes in pH, metal concentration and other characteristics of the microenvironment. The desirable properties of these functionalized dyes are due to a core structure with highly π -conjugated and

aryl systems in which electrons are delocalized. This reduces the energy needed for light excitation. These small-molecule dyes are the optoacoustic imaging probes of choice because of their strong contrast (due to relatively sharp absorption peaks), rapid clearance, low toxicity, and favorable biocompatibility. Despite these advantages, small-molecule dyes also present several challenges: their molar extinction coefficients are much lower than those of polymeric and inorganic imaging probes, they photobleach easily and they tend to aggregate. Aggregation can be reduced by incorporating hydrophylic groups, tripletstate quenchers and stabilizing groups.

3. Genetically engineered chromophores

Genetically encoded chromophores, such as reporter gene systems, offer unique advantages over exogenous and other endogenous chromophores. They offer advantages over exogenous chromophores because they are expressed in situ and they can be expressed over extended periods, allowing longitudinal studies. They offer advantages over other endogenous chromophores, such as hemoglobin, because they can label a broad array of biological processes and can be customized through genetic engineering to ensure adequate physicochemical properties for optoacoustic imaging. Several genetically engineered chromophores can be expressed and monitored in desired tissues; these

include fluorescent proteins such as enhanced green fluorescent protein (eGFP), bacteriophytochrome-based near-infrared fluorescent protein (iRFP), and mCherry; non-fluorescent proteins such as the LacZ-encoded β-galactosidase; and melanin, the production of which can be controlled by regulating tyrosinase activity.9,168-173

Razansky and colleagues visualized eGFP at high resolution in living Drosophila melanogaster using MSOT. 168 The Gal-4/UAS system was used to express eGFP in the salivary glands, which were illuminated at three wavelengths; the resulting optoacoustic images were recorded and processed. The authors also used the Gal-4/UAS system in zebrafish to express mCherry in the vertebral column. The optoacoustic images of mCherry at three wavelengths showed strong contrast from absorption in the vertebral column and surrounding tissue (Fig. 7(1)). Imaging of mCherry in the zebrafish head allowed analysis of morphological features. This work showed, for the first time, that MSOT can detect fluorescent proteins in vivo, with a penetration limit extending well beyond the limit of optical microscopy. This reporter system may allow the use of optoacoustic imaging to study signaling pathways, gene expression, morphogenesis, and disease progression. Using iRFP as a probe, Filonov and colleagues showed that it could generate a strong optoacoustic signal after excitation at 680 nm. 170 This chromophore has absorption and emission spectra within the NIR range, a very high intrinsic extinction coefficient of 105 000 M⁻¹ cm⁻¹ and a fluorescence quantum yield of only 6%. The authors expressed

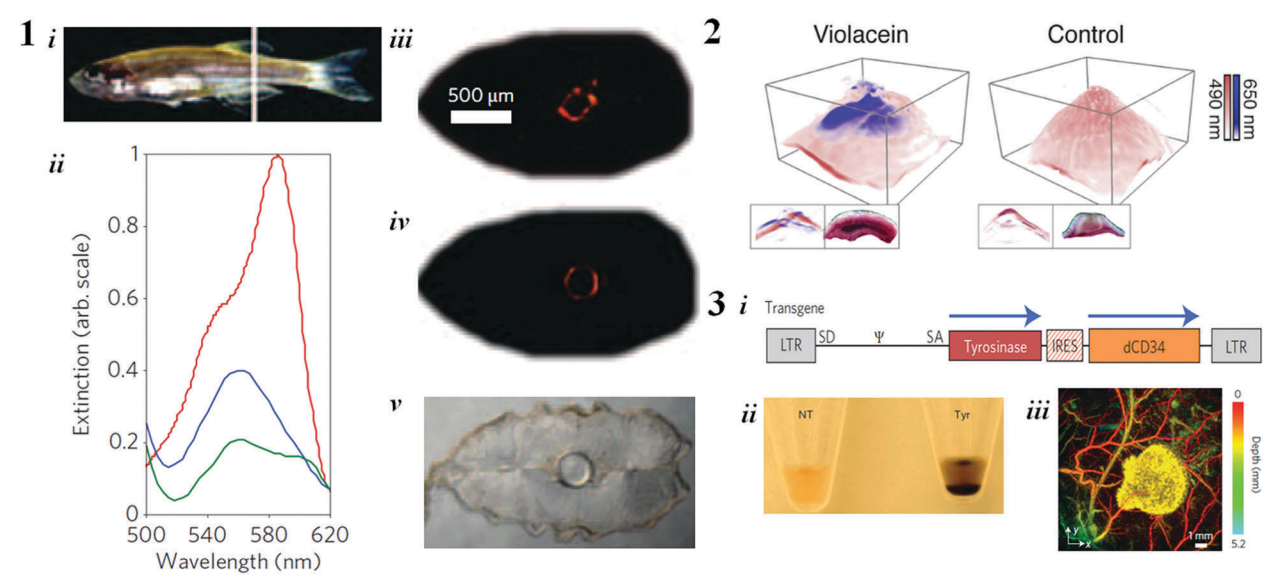


Fig. 7 (1) Imaging of mCherry distribution in the vertebral column of an adult zebrafish. (i) Location of the imaging plane. (ii) Extinction spectra of mCherry (red) and intrinsic background (vertebral column, blue; muscles, green). (iii) Spectrally resolved image of mCherry distribution. (iv) Histological epifluorescence image of dissected tissue, showing the mCherry-expressing vertebral column in red. (v) Histological section. Reprinted with permission from ref. 168. Copyright 2009, Nature Publishing Group. (2) In vivo optoacoustic imaging of 4T1 tumors containing Violacein-expressing (left) or nonexpressing bacteria (right). The upper part of the panel shows 3D views, while the lower part shows an optoacoustic axial cross section through the center of the volume on the left, next to the corresponding cryosection on the right, where E. coli were specifically stained using a molecular chromophore. Reprinted with permission from ref. 174. Copyright 2015, Nature Publishing Group. (3) (i) Schematic of the tyrosinase-expressing transgene engineered into retrovirus to drive expression of eumelanin in infected host cells. Tyr, human tyrosinase; IRES, internal ribosome entry site; dCD34, truncated human CD34; LTR, long terminal repeat. (iii) Pigmentation of pelleted 293T cells infected with the transgene. (iii) Optoacoustic images of tyrosinase-expressing K562 cells after subcutaneous injection into the flank of a nude mouse. Vasculature is colored by depth; a K562 cell is shown in yellow. Reprinted with permission from ref. 181. Copyright 2015, Nature Publishing Group.

the chromophore in MTLn3 cells and injected them into mice. Xenografts were imaged at 2 and 3 weeks after implantation. Spectrally resolved, high-contrast volumetric images of tumors were obtained at depths down to 4 mm using photoacoustic computed tomography and deep-photoacoustic microscopy.

ChemComm

Jiang and colleagues reported Violacein, a biosynthetic probe for optoacoustic imaging of living bacteria. They developed an *E. coli* strain carrying the operon of enzymes needed for Violacein synthesis. The probe was synthesized rapidly, and it showed good, photobleaching-resistant optoacoustic contrast even after 25 000 pulses. When mice with xenograft tumors were infected with bacteria expressing this probe, the bacteria were easily detected in tumors using MSOT, reflecting the photobleaching resistance of the probe (Fig. 7(2)). The authors further demonstrated the anti-cancer activity of purified Violacein *in vitro*, raising the possibility of theranostic applications.

Stritzker and colleagues reported the use of virus-driven melanin production for theranostics, including as a marker during surgery, endoscopy, optoacoustic or magnetic resonance imaging, or photothermotherapy induced by NIR light. The authors generated a recombinant oncolytic vaccinia virus that inserts the tyrosinase gene into host cells, causing them to express the pigment eumelanin. This pigment produces strong optoacoustic contrast because it is highly photostable and absorbs strongly at longer wavelengths than hemoglobin does. 172,173,175-177 When the authors infected lung carcinoma A549 cells and prostate cancer PC3 cells with the recombinant vaccinia virus, strong optoacoustic signals in the NIR range were observed. Optoacoustic imaging of tumors grown in mice from these infected cells revealed abundant melanin deep within the tumors and lymph nodes. The melanin expressed by the vaccinia-infected PC3 tumors shows therapeutic possibilities: the pigment's strong absorption in the NIR range led to sufficient local heating in the tumor to induce cell death and tumor shrinkage. 175 Extending the use of recombinant vaccinia virus to express melanin, Kirscher and colleagues reported a doxycycline-inducible melanin production system for cancer therapy and magnetic resonance imaging and MSOT of tumor tissues. 178 Inducible melanin expression was achieved by inserting the tet-regulated gene expression system into the vaccinia genome. 175 Adding doxycycline to A549 or PANC-1 cancer cells or tumors infected with the recombinant virus led to sufficient melanin production to allow detection by magnetic resonance imaging and MSOT. The possibility of inducible melanin synthesis may be useful for precise cancer imaging and photothermotherapy. Melanin may also be useful as a probe in magnetic resonance imaging, since melanomas show strong signals on T_1 -weighted magnetic resonance images. ^{179,180}

Along similar lines, Jathoul and colleagues engineered a recombinant retrovirus to coexpress tyrosinase with a cell surface marker (dCD34) and thereby drive synthesis of eumelanin (Fig. 7(3)). They infected a variety of cell lines with this virus and selected a cell line stably expressing eumelanin. They imaged transduced cells with a highly sensitive Fabry-Perot ultrasound detector. The cells appeared black to the eye, and illuminating them with 30 000 laser pulses at a fluence of 1.7 mJ cm⁻² at 50 Hz generated optoacoustic signals that

remained stable for 1 h. Implanting transduced K562 cells subcutaneously into mice and illuminating the tissue at 600 nm revealed the grafted cells and surrounding vasculature with excellent contrast, which was even higher when the tissue was illuminated at wavelengths beyond 650 nm, where eumelanin continues to absorb strongly while absorption by blood falls off. Similar results were observed when mice were implanted with transduced human embryonic kidney 293T cells. In these ways, this eumelanin system offers robustness, because transduction is stable; signal amplification, because eumelanin can be expressed at high levels; and faster data acquisition, because images can be obtained at single wavelengths beyond 650 nm. The fact that melanin can chelate radioactive or magnetic metal ions raises the potential of multimodal imaging. ^{72,182,183}

Inducible genetically engineered chromophores were explored by Yao and colleagues, who reported a reversibly activatable photoresponsive bacterial phytochrome (BphP1). 184 Nonfluorescent BphP1 absorbs light at 600-800 nm, and its absorption spectrum shows substantial red-shifting, allowing it to transmit molecular information from deep within tissue. Binding of BphP1 to biliverdin shifts BphP1 from a red-absorbing state to an NIR-absorbing one, and this switch reverses upon biliverdin dissociation. As a result, BphP1 undergoes a photoconversion from an "on" to "off" state upon illumination at 730-790 nm, and it undergoes the reverse photoconversion upon illumination at 630-690 nm. The authors tested the performance of BphP1 in vivo by injecting BphP1-expressing U87 cells into the left kidney to induce tumor growth. The molar extinction coefficient of BphP1 in the "on" state with illumination at 780 nm was \sim 70-fold higher than that of oxyhemoglobin, while the coefficient in the "off" state at 630 nm was \sim 40-fold higher. The photoswitching ability of BphP1 at 630 nm and 780 nm was observed even at depths of \sim 8 mm. In separate experiments, the authors showed that BphP1-expressing U87 tumors were detectable in mouse brain at \sim 3 mm beneath the scalp surface. In a further demonstration of the potential of combining photoactivatable probes with optoacoustic imaging for deep tissue monitoring, Stiel and colleagues reported MSOT of reversibly activatable fluorescent proteins Dronpa and its M159T variant. 185 The authors were able to resolve the simultaneous switches in optoacoustic signal trajectories of the two proteins.

The potential for rapid development of non-invasive dynamic sensing using reversibly activatable MSOT probes was demonstrated most recently by Deán-Ben and colleagues, who expressed the calcium indicator GCaMP5G in neurons of zebrafish and then tracked the optoacoustic signal in immobilized and freely swimming larvae as well as in adult brains. ¹⁸⁶ The authors demonstrated that large changes in GCaMP5G fluorescence were reflected in the optoacoustic signal, and they were able to track neural dynamics using so-called functional optoacoustic neurotomography (FONT). The ability to follow neural changes in living, unrestrained organisms using dynamic MSOT raises new possibilities for neurobiological and neurochemical studies.

The array of genetically engineered chromophores for optoacoustic imaging clearly indicates that these chromophores **Feature Article**

may help us to understand the biology of different diseases, such as through the visualization of tumor cell populations and the analysis of molecular and cellular processes, tumor growth, metastasis and response to therapy. Reporter gene systems offer several advantages over chemical probes: it is relatively easy and cost-effective to express genes, even on a large scale; the protein products can be selected to allow interrogation of a range of molecular events, such as gene expression, signal transduction, and protein-protein or protein-drug interactions; and biological phenomena can be monitored longitudinally within the same animal, potentially increasing reproducibility. The fact that these chromophores are expressed in situ means that their local concentrations can provide good optoacoustic signals and can remain stable in space and time, allowing repeated imaging over time. Although the feasibility of performing reporter gene-based imaging of humans remains unclear, Jacobs and colleagues demonstrated the possibility of PETimaging based on HSV-1-tk expression in glioblastoma patients, a system that may help to predict effects of gene therapy. 187,188 One challenge to creating reporter systems for humans is developing human vectors that can target specific tissues, allowing tissue-specific imaging. Further work is needed to develop spatiotemporal control over expression of these chromophores in order to expand the possibilities for imaging entire tissues, specific subregions or specific cell types. Further work is also needed to refine the control of chromophore expression levels, since overexpression can affect the growth of expressing cells and even trigger toxic effects and immune responses. At the moment, the possibilities for dynamic sensing are limited to tens of milliseconds, which is how long it takes for GCaMPs to respond to action potential-induced calcium influx. 186 Future work should aim to accelerate the kinetics of sensing as well as

4. Perspectives and future directions

optimize MSOT probes for clinically relevant applications.

Optoacoustic imaging is a fast-developing imaging modality with significant potential applications in the life sciences. It offers higher resolution than conventional optical macroscopy methods and can be safely applied *in vivo* since it uses nonionizing radiation. Label-free imaging based on endogenous absorbers can provide anatomical and functional information on tissues, enabling unique tissue observations. However, visualization of an extended profile of physiological, cellular and molecular parameters requires the use of exogenous photoabsorbing agents. Advantageously, MSOT can distinguish absorbers of different spectral signatures, allowing concurrent imaging of multiple biological processes.

Here we have reviewed classes of imaging probes for use in MSOT applications. Polymeric and inorganic imaging probes feature high molar extinction coefficients, tunable peak absorption wavelengths, and good photo-stability, and they can be produced with desirable circulation times (half-lives). In contrast, inorganic probes pose a challenge because they are not biodegradable and so are not excreted from the body, raising

the risk of toxicity. Small-molecule organic dyes are typically excreted quickly via the renal pathway, so they raise fewer toxicity concerns. On the other hand, small-molecule dyes can suffer from photobleaching and degradation. The biodistribution and toxicity profile of the agents reviewed here must be considered carefully with the aim of clinical application. Future studies may need to focus on optimizing chromophore properties (size, charge, surface characteristics) in order to reduce toxicity, improve biocompatibility, and confer the ability to target specific tissues or sense specific changes in the microenvironment. In parallel, such optimization studies should focus on ensuring (1) easy and cost-effective synthesis, (2) hydrophilicity for intravenous administration, (3) good half-life and photostability, and (4) high efficiency at converting light to ultrasound. It is our hope that this review will stimulate greater efforts towards the conscious design of MSOT probes, which may help advance the field faster than relying on "re-purposed" probes originally optimized for optical imaging modalities.

Like the authors of recent reviews, 13,14 we believe that activatable imaging probes can play a key role in sensing dynamic changes in enzyme activity, pH, pO2 or ROS and ion levels. MSOT is ideal for such dynamic sensing studies, since its spectral unmixing procedure can distinguish signals from the different states of an activatable probe, as well as distinguish signals from probe and background absorbers. On the basis of our review, we suggest that development of such probes may wish to focus on two mechanisms. One is the surface plasmon resonance effect as observed with gold nanoparticles. In plasmonic (noble metal) nanoparticles, strong electromagnetic fields on the particle surface increase all radiative properties, including absorption. 189 This mechanism can be useful for designing reversibly activatable probes. A second mechanism that emerges from our review is the addition of a targeting peptide to probe nanostructures; enzyme cleavage of this peptide in situ triggers probe aggregation that enhances the optoacoustic signal. 156 This mechanism may be useful for designing irreversibly activatable probes.

Small-molecule dyes may be even better suited than polymeric and inorganic imaging probes to sensing the microenvironment of receptors, proteins, and enzymes. Activatable probes require two essential features: a target-binding, sensing moiety; and a fluorochrome backbone capable of absorbing photons. The target-binding moiety should be directly connected to the fluorochrome and the electronic or molecular structure of the probe should change upon interaction with the target, giving rise to a change in optoacoustic signal. An example of a change in the electronic structure is the reversible transfer of electrons upon calcium chelation. 154 An example of a change in the molecular structure is Cu²⁺-activated irreversible bond cleavage that leads to ratiometric optoacoustic signal enhancement. 157 Another possibility is to enhance optoacoustic signals using Förster resonance energy transfer (FRET): addition of a quencher to a solution containing the fluorophore (donor) reduces donor emission and increases the optoacoustic signal. 190 In this approach, the donor and quencher should be connected at an optimal separation via a target-binding linker. Depending on

the target, this strategy could be used to design reversible and irreversible activatable probes.

Although small molecules allow flexibility for generating optoacoustic probes, some chromophoric backbones offer poor optoacoustic contrast because their molar extinction coefficients are much lower than those of polymeric nanostructures or inorganic nanoparticles. Thus, future work should aim to synthesize probes based on activatable small-molecule dyes. This may lead not only to significantly stronger optoacoustic signals but also to longer persistence in the blood stream as well as better biodegradability.

Another key area of research is the development of reporter genes for optoacoustic imaging. We have only begun to exploit the power of biotechnology to generate optoacoustic contrast in cells and tissues in healthy or diseased states. Genetically engineered proteins may provide the optoacoustic equivalent of green fluorescent protein and can become essential in MSOT-based biological discovery. Genetically engineered proteins can reversibly alter their optoacoustic signals upon target sensing, as a result of FRET191 or as a result of conformational changes such as in the calcium indicator GCaMP5G186 or the photoswitchable Dronpa and its M159T variant. 185 Combining multiple genes or chimeric fusions may be particularly useful for multimodal imaging. Although the clinical potential of reporter gene systems remains to be demonstrated, studies already suggest its feasibility. 187,188 In parallel, advances in optoacoustic imaging technology in terms of laser repetition rate, detection sensitivity and quantitative spectral differentiation algorithms can help further optimize the use of optoacoustic probes. In particular, advanced algorithms have recently been developed to improve the detection sensitivity and specificity of spectral signatures in tissues. 28,32,192

Overall, the combination of new classes of probes offering strong optoacoustic contrast and of adept, sensitive MSOT systems may enable optical imaging of biological contrast at higher resolution and deeper in tissue than has been possible using optical techniques.

Notes and references

- 1 B. Amos, Nat. Cell Biol., 2000, 2, E151-E152.
- 2 M. L. James and S. S. Gambhir, Physiol. Rev., 2012, 92, 897-965.
- 3 V. Ntziachristos, Nat. Methods, 2010, 7, 603-614.
- 4 R. Y. Tsien, FEBS Lett., 2005, 579, 927-932.
- 5 R. Y. Tsien, Integr. Biol., 2010, 2, 77-93.
- 6 B. N. Giepmans, S. R. Adams, M. H. Ellisman and R. Y. Tsien, Science, 2006, 312, 217-224.
- 7 M. J. Whitley, D. M. Cardona, A. L. Lazarides, I. Spasojevic, J. M. Ferrer, J. Cahill, C. L. Lee, M. Snuderl, D. G. Blazer, E. S. Hwang, R. A. Greenup, P. J. Mosca, J. K. Mito, K. C. Cuneo, N. A. Larrier, E. K. O'Reilly, R. F. Riedel, W. C. Eward, D. B. Strasfeld, D. Fukumura, R. K. Jain, W. D. Lee, L. G. Griffith, M. G. Bawendi, D. G. Kirsch and B. E. Brigman, Sci. Transl. Med., 2016, 8, 320320ra4.
- 8 A. Ale, V. Ermolayev, E. Herzog, C. Cohrs, M. H. de Angelis and V. Ntziachristos, *Nat. Methods*, 2012, **9**, 615–620.
- 9 G. M. van Dam, G. Themelis, L. M. A. Crane, N. J. Harlaar, R. G. Pleijhuis, W. Kelder, A. Sarantopoulos, J. S. de Jong, H. J. G. Arts, A. G. J. van der Zee, J. Bart, P. S. Low and V. Ntziachristos, *Nat. Med.*, 2011, 17, 1315–U1202.
- 10 B. E. Schaafsma, J. S. D. Mieog, M. Hutteman, J. R. Van der Vorst, P. J. K. Kuppen, C. W. G. M. Lowik, J. V. Frangioni, C. J. H. Van de Velde and A. L. Vahrmeijer, J. Surg. Oncol., 2011, 104, 323–332.

11 C. Chi, Y. Du, J. Ye, D. Kou, J. Qiu, J. Wang, J. Tian and X. Chen, Theranostics, 2014, 4, 1072–1084.

- 12 L. Azizi, K. Zarychta, D. Ettori, E. Tinet and J. M. Tualle, Opt. Express, 2009, 17, 12132–12144.
- 13 J. Weber, P. C. Beard and S. E. Bohndiek, Nat. Methods, 2016, 13, 639–650.
- 14 L. Nie and X. Chen, Chem. Soc. Rev., 2014, 43, 7132-7170.
- 15 A. Rosencwaig and A. Gersho, J. Appl. Phys., 1976, 47, 64.
- 16 R. A. Kruger, K. D. Miller, H. E. Reynolds, W. L. Kiser, D. R. Reinecke and G. A. Kruger, *Radiology*, 2000, 216, 279–283.
- 17 X. D. Wang, Y. J. Pang, G. Ku, X. Y. Xie, G. Stoica and L. H. V. Wang, Nat. Biotechnol., 2003, 21, 803–806.
- 18 V. Ntziachristos, J. Ripoll, L. H. V. Wang and R. Weissleder, *Nat. Biotechnol.*, 2005, 23, 313–320.
- 19 V. Ntziachristos and D. Razansky, Chem. Rev., 2010, 110, 2783-2794.
- 20 S. Zackrisson, S. M. van de Ven and S. S. Gambhir, Cancer Res., 2014, 74, 979–1004.
- 21 J. Prakash, A. S. Raju, C. B. Shaw, M. Pramanik and P. K. Yalavarthy, Biomed. Opt. Express, 2014, 5, 1363–1377.
- 22 A. Rosenthal, V. Ntziachristos and D. Razansky, Curr. Med. Imaging Rev., 2013, 9, 318–336.
- 23 R. Weissleder and V. Ntziachristos, Nat. Med., 2003, 9, 123-128.
- 24 A. Taruttis and V. Ntziachristos, Nat. Photonics, 2015, 9, 219-227.
- 25 M. Omar, M. Schwarz, D. Soliman, P. Symvoulidis and V. Ntziachristos, Neoplasia, 2015, 17, 208–214.
- 26 S. Mandal, X. L. Dean-Ben, N. C. Burton and D. Razansky, *IEEE Pulse*, 2015, 6, 47–53.
- 27 A. Buehler, M. Kacprowicz, A. Taruttis and V. Ntziachristos, Opt. Lett., 2013, 38, 1404–1406.
- 28 S. Tzoumas, A. Nunes, I. Olefir, S. Stangl, P. Symvoulidis, S. Glasl, C. Bayer, G. Multhoff and V. Ntziachristos, *Nat. Commun.*, 2016, 7, 12121.
- 29 P. Mohajerani, S. Tzoumas, A. Rosenthal and V. Ntziachristos, *IEEE Signal Proc. Mag.*, 2015, 32, 88–100.
- 30 E. Herzog, A. Taruttis, N. Beziere, A. A. Lutich, D. Razansky and V. Ntziachristos, *Radiology*, 2012, **263**, 461–468.
- 31 I. Stoffels, S. Morscher, I. Helfrich, U. Hillen, J. Lehy, N. C. Burton, T. C. P. Sardella, J. Claussen, T. D. Poeppel, H. S. Bachmann, A. Roesch, K. Griewank, D. Schadendorf, M. Gunzer and J. Klode, Sci. Transl. Med., 2015, 7, 317ra199.
- 32 S. Tzoumas, N. C. Deliolanis, S. Morscher and V. Ntziachristos, *IEEE Trans. Med. Imaging*, 2014, 33, 48-60.
- 33 A. Chekkoury, A. Nunes, J. Gateau, P. Symvoulidis, A. Feuchtinger, N. Beziere, S. V. Ovsepian, A. Walch and V. Ntziachristos, *Neoplasia*, 2016, 18, 459–467.
- 34 M. Gerling, Y. Zhao, S. Nania, K. J. Norberg, C. S. Verbeke, B. Englert, R. V. Kuiper, A. Bergstrom, M. Hassan, A. Neesse, J. M. Lohr and R. L. Heuchel, *Theranostics*, 2014, 4, 604–613.
- 35 L. J. Rich and M. Seshadri, Sci. Rep., 2016, 6, 21237.
- 36 P. Beard, Interface Focus, 2011, 1, 602-631.
- 37 D. Razansky, C. Vinegoni and V. Ntziachristos, Opt. Lett., 2007, 32, 2891–2893.
- 38 S. Tzoumas, A. Nunes, N. C. Deliolanis and V. Ntziachristos, *J. Biophotonics*, 2015, **8**, 629–637.
- 39 A. Taruttis, M. Wildgruber, K. Kosanke, N. Beziere, K. Licha, R. Haag, M. Aichler, A. Walch, E. Rummeny and V. Ntziachristos, *Photoacoustics*, 2013, 1, 3–8.
- 40 J. Dernedde, A. Rausch, M. Weinhart, S. Enders, R. Tauber, K. Licha, M. Schirner, U. Zugel, A. von Bonin and R. Haag, *Proc. Natl. Acad. Sci. U. S. A.*, 2010, 107, 19679–19684.
- 41 K. Licha, P. Welker, M. Weinhart, N. Wegner, S. Kern, S. Reichert, I. Gemeinhardt, C. Weissbach, B. Ebert, R. Haag and M. Schirner, *Bioconjugate Chem.*, 2011, 22, 2453–2460.
- 42 E. Abbasi, S. F. Aval, A. Akbarzadeh, M. Milani, H. T. Nasrabadi, S. W. Joo, Y. Hanifehpour, K. Nejati-Koshki and R. Pashaei-Asl, *Nanoscale Res. Lett.*, 2014, **9**, 247.
- 43 Z. B. Zha, Z. J. Deng, Y. Y. Li, C. H. Li, J. R. Wang, S. M. Wang, E. Z. Qu and Z. F. Dai, *Nanoscale*, 2013, 5, 4462–4467.
- 44 J. Jang and H. Yoon, Small, 2005, 1, 1195-1199.
- 45 J. Y. Hong, H. Yoon and J. Jang, Small, 2010, 6, 679-686.
- 46 Z. B. Zha, X. L. Yue, Q. S. Ren and Z. F. Dai, *Adv. Mater.*, 2013, 25, 777–782.
- 47 W. Lu, Q. Huang, K. B. Geng, X. X. Wen, M. Zhou, D. Guzatov, P. Brecht, R. Su, A. Oraevsky, L. V. Wang and C. Li, *Biomaterials*, 2010, 31, 2617–2626.

- 48 S. Prahl, OMLC. Online. 1998. URL: http://omlc.ogi.edu/spectra/hemoglobin/.
- 49 J. Liu, J. L. Geng, L. D. Liao, N. Thakor, X. H. Gao and B. Liu, *Polym. Chem.*, 2014, 5, 2854–2862.
- 50 G. Balasundaram, C. J. H. Ho, K. Li, W. Driessen, U. S. Dinish, C. L. Wong, V. Ntziachristos, B. Liu and M. Olivo, *Int. J. Nanomed.*, 2015, 10, 387–397.
- 51 J. F. Lovell, C. S. Jin, E. Huynh, H. L. Jin, C. Kim, J. L. Rubinstein, W. C. W. Chan, W. G. Cao, L. V. Wang and G. Zheng, *Nat. Mater.*, 2011, 10, 324–332.
- 52 E. Huynh, C. S. Jin, B. C. Wilson and G. Zheng, *Bioconjugate Chem.*, 2014, 25, 796–801.
- 53 E. Huynh, B. Y. C. Leung, B. L. Helfield, M. Shakiba, J. A. Gandier, C. S. Jin, E. R. Master, B. C. Wilson, D. E. Goertz and G. Zheng, *Nat. Nanotechnol.*, 2015, 10, 325–332.
- 54 K. K. Ng, M. Shakiba, E. Huynh, R. A. Weersink, A. Roxin, B. C. Wilson and G. Zheng, ACS Nano, 2014, 8, 8363–8373.
- 55 C. S. Jin, J. F. Lovell, J. Chen and G. Zheng, ACS Nano, 2013, 7, 2541–2550.
- 56 C. S. Jin, L. Y. Cui, F. Wang, J. Chen and G. Zheng, Adv. Healthcare Mater., 2014, 3, 1240–1249.
- 57 E. Huynh and G. Zheng, Nano Today, 2014, 9, 212-222.
- 58 J. Mei, Y. Diao, A. L. Appleton, L. Fang and Z. Bao, *J. Am. Chem. Soc.*, 2013, **135**, 6724–6746.
- 59 J. Peet, J. Y. Kim, N. E. Coates, W. L. Ma, D. Moses, A. J. Heeger and G. C. Bazan, *Nat. Mater.*, 2007, **6**, 497–500.
- 60 A. Rose, Z. Zhu, C. F. Madigan, T. M. Swager and V. Bulovic, *Nature*, 2005, 434, 876–879.
- 61 C. Wu and D. T. Chiu, Angew. Chem., Int. Ed. Engl., 2013, 52, 3086-3109.
- 62 K. Y. Pu and B. Liu, Adv. Funct. Mater., 2011, 21, 3408-3423.
- 63 K. Y. Pu, A. J. Shuhendler, J. V. Jokerst, J. G. Mei, S. S. Gambhir, Z. N. Bao and J. H. Rao, *Nat. Nanotechnol.*, 2014, 9, 233–239.
- 64 A. de Vries, E. Custers, J. Lub, S. van den Bosch, K. Nicolay and H. Grull, *Biomaterials*, 2010, 31, 6537–6544.
- 65 Q. Yin, F. Y. Yap, L. C. Yin, L. Ma, Q. Zhou, L. W. Dobrucki, T. M. Fan, R. C. Gaba and J. J. Cheng, J. Am. Chem. Soc., 2013, 135, 13620–13623.
- 66 E. D. Pressly, R. A. Pierce, L. A. Connal, C. J. Hawker and Y. J. Liu, Bioconjugate Chem., 2013, 24, 196–204.
- 67 D. Ding, K. Li, Z. S. Zhu, K. Y. Pu, Y. Hu, X. Q. Jiang and B. Liu, Nanoscale, 2011, 3, 1997–2002.
- 68 X. L. Feng, F. T. Lv, L. B. Liu, H. W. Tang, C. F. Xing, Q. O. Yang and S. Wang, ACS Appl. Mater. Interfaces, 2010, 2, 2429–2435.
- 69 P. Howes, M. Green, J. Levitt, K. Suhling and M. Hughes, J. Am. Chem. Soc., 2010, 132, 3989–3996.
- 70 K. Y. Pu, N. Chattopadhyay and J. H. Rao, J. Controlled Release, 2016, 240, 312–322.
- 71 Q. L. Fan, K. Cheng, X. Hu, X. W. Ma, R. P. Zhang, M. Yang, X. M. Lu, L. Xing, W. Huang, S. S. Gambhir and Z. Cheng, *J. Am. Chem. Soc.*, 2014, **136**, 15185–15194.
- 72 L. Hong and J. D. Simon, J. Phys. Chem. B, 2007, 111, 7938-7947.
- 73 M. L. Janssen, W. J. Oyen, I. Dijkgraaf, L. F. Massuger, C. Frielink, D. S. Edwards, M. Rajopadhye, H. Boonstra, F. H. Corstens and O. C. Boerman, *Cancer Res.*, 2002, 62, 6146–6151.
- 74 R. P. Zhang, Q. L. Fan, M. Yang, K. Cheng, X. M. Lu, L. Zhang, W. Huang and Z. Cheng, Adv. Mater., 2015, 27, 5063–5069.
- 75 J. M. Llovet, S. Ricci, V. Mazzaferro, P. Hilgard, E. Gane, J. F. Blanc, A. C. de Oliveira, A. Santoro, J. L. Raoul, A. Forner, M. Schwartz, C. Porta, S. Zeuzem, L. Bolondi, T. F. Greten, P. R. Galle, J. F. Seitz, I. Borbath, D. Haussinger, T. Giannaris, M. Shan, M. Moscovici, D. Voliotis, J. Bruix and S. I. S. Grp, N. Engl. J. Med., 2008, 359, 378–390.
- 76 M. C. Daniel and D. Astruc, Chem. Rev., 2004, 104, 293-346.
- 77 K. A. Willets and R. P. Van Duyne, Annu. Rev. Phys. Chem., 2007, 58, 267–297.
- 78 A. Taruttis, E. Herzog, D. Razansky and V. Ntziachristos, Opt. Express, 2010, 18, 19592–19602.
- 79 E. Petryayeva and U. J. Krull, *Anal. Chim. Acta*, 2011, **706**, 8–24.
- 80 L. Cavigli, M. de Angelis, F. Ratto, P. Matteini, F. Rossi, S. Centi, F. Fusi and R. Pini, *J. Phys. Chem. C*, 2014, **118**, 16140–16146.
- 81 J. V. Jokerst, A. J. Cole, D. Van de Sompel and S. S. Gambhir, ACS Nano, 2012, 6, 10366–10377.
- 82 P. K. Jain and M. A. El-Sayed, Chem. Phys. Lett., 2010, 487, 153-164.

- 83 A. Sanchez-Iglesias, M. Grzelczak, J. Perez-Juste and L. M. Liz-Marzan, Angew. Chem., Int. Ed., 2010, 49, 9985–9989.
- 84 J. Comenge, O. Fragueiro, J. Sharkey, A. Taylor, M. Held, N. C. Burton, B. K. Park, B. Wilm, P. Murray, M. Brust and R. Levy, ACS Nano, 2016, 10, 7106–7116.
- 85 Y. S. Chen, W. Frey, S. Kim, P. Kruizinga, K. Homan and S. Emelianov, *Nano Lett.*, 2011, 11, 348–354.
- 86 N. Lozano, W. T. Al-Jamal, A. Taruttis, N. Beziere, N. C. Burton, J. Van den Bossche, M. Mazza, E. Herzog, V. Ntziachristos and K. Kostarelos, J. Am. Chem. Soc., 2012, 134, 13256–13258.
- 87 A. Taruttis, N. Lozano, A. Nunes, D. A. Jasim, N. Beziere, E. Herzog, K. Kostarelos and V. Ntziachristos, *Nanoscale*, 2014, 6, 13451–13456.
- 88 C. C. Bao, N. Beziere, P. del Pino, B. Pelaz, G. Estrada, F. R. Tian, V. Ntziachristos, J. M. de la Fuente and D. X. Cui, *Small*, 2013, 9, 68-74.
- 89 Y. J. Liu, J. He, K. K. Yang, C. L. Yi, Y. Liu, L. M. Nie, N. M. Khashab, X. Y. Chen and Z. H. Nie, Angew. Chem., Int. Ed., 2015, 54, 15809–15812.
- 90 J. Vonnemann, N. Beziere, C. Bottcher, S. B. Riese, C. Kuehne, J. Dernedde, K. Licha, C. von Schacky, Y. Kosanke, M. Kimm, R. Meier, V. Ntziachristos and R. Haag, *Theranostics*, 2014, 4, 629–641.
- 91 M. Weinhart, D. Groger, S. Enders, J. Dernedde and R. Haag, *Biomacromolecules*, 2011, 12, 2502–2511.
- 92 S. Hirn, M. Semmler-Behnke, C. Schleh, A. Wenk, J. Lipka, M. Schaffler, S. Takenaka, W. Moller, G. Schmid, U. Simon and W. G. Kreyling, Eur. J. Pharm. Biopharm., 2011, 77, 407–416.
- 93 M. Zhang, M. Yudasaka, K. Ajima, J. Miyawaki and S. Iijima, ACS Nano, 2007, 1, 265–272.
- 94 B. Tian, C. Wang, S. Zhang, L. Z. Feng and Z. Liu, ACS Nano, 2011, 5, 7000-7009.
- 95 K. Yang, L. Z. Feng, X. Z. Shi and Z. Liu, Chem. Soc. Rev., 2013, 42, 530–547.
- 96 P. F. Rong, K. Yang, A. Srivastan, D. O. Kiesewetter, X. Y. Yue, F. Wang, L. M. Nie, A. Bhirde, Z. Wang, Z. Liu, G. Niu, W. Wang and X. Y. Chen, *Theranostics*, 2014, 4, 229–239.
- 97 D. Y. Pan, J. C. Zhang, Z. Li and M. H. Wu, Adv. Mater., 2010, 22, 734–738.
- 98 X. J. Zhou, Y. Zhang, C. Wang, X. C. Wu, Y. Q. Yang, B. Zheng, H. X. Wu, S. W. Guo and J. Y. Zhang, ACS Nano, 2012, 6, 6592–6599.
- 99 K. Erickson, R. Erni, Z. Lee, N. Alem, W. Gannett and A. Zettl, Adv. Mater., 2010, 22, 4467–4472.
- 100 J. L. Li, K. N. Kudin, M. J. McAllister, R. K. Prud'homme, I. A. Aksay and R. Car, *Phys. Rev. Lett.*, 2006, **96**, 176101–176104.
- 101 L. Zhang, J. J. Liang, Y. Huang, Y. F. Ma, Y. Wang and Y. S. Chen, Carbon, 2009, 47, 3365–3368.
- 102 K. J. Ziegler, Z. N. Gu, H. Q. Peng, E. L. Flor, R. H. Hauge and R. E. Smalley, *J. Am. Chem. Soc.*, 2005, **127**, 1541–1547.
- 103 M. A. Patel, H. Yang, P. L. Chiu, D. D. Mastrogiovanni, C. R. Flach, K. Savaram, L. Gomez, A. Hemnarine, R. Mendelsohn, E. Garfunkel, H. Jiang and H. He, ACS Nano, 2013, 7, 8147–8157.
- 104 K. Yang, L. L. Hu, X. X. Ma, S. Q. Ye, L. Cheng, X. Z. Shi, C. H. Li, Y. G. Li and Z. Liu, Adv. Mater., 2012, 24, 1868–1872.
- 105 Z. Liu, W. B. Cai, L. N. He, N. Nakayama, K. Chen, X. M. Sun, X. Y. Chen and H. J. Dai, *Nat. Nanotechnol.*, 2007, 2, 47–52.
- 106 A. Bianco, K. Kostarelos and M. Prato, Curr. Opin. Chem. Biol., 2005, 9, 674-679.
- 107 S. S. Li, H. He, Q. C. Jiao and P. H. Chuong, *Prog. Chem.*, 2008, 20, 1798–1803.
- 108 W. X. Zhang, Z. Z. Zhang and Y. G. Zhang, Nanoscale Res. Lett., 2011, 6, 555.
- 109 A. De La Zerda, C. Zavaleta, S. Keren, S. Vaithilingam, S. Bodapati, Z. Liu, J. Levi, B. R. Smith, T. J. Ma, O. Oralkan, Z. Cheng, X. Y. Chen, H. J. Dai, B. T. Khuri-Yakub and S. S. Gambhir, *Nat. Nanotechnol.*, 2008, 3, 557–562.
- 110 A. de la Zerda, S. Bodapati, R. Teed, S. Y. May, S. M. Tabakman, Z. Liu, B. T. Khuri-Yakub, X. Chen, H. Dai and S. S. Gambhir, ACS Nano, 2012, 6, 4694–4701.
- 111 J. W. Kim, E. I. Galanzha, E. V. Shashkov, H. M. Moon and V. P. Zharov, *Nat. Nanotechnol.*, 2009, 4, 688–694.
- 112 K. Yang, L. Zhu, L. M. Nie, X. L. Sun, L. Cheng, C. X. Wu, G. Niu, X. Y. Chen and Z. Liu, *Theranostics*, 2014, 4, 134–141.
- 113 J. Levi, S. R. Kothapalli, T. J. Ma, K. Hartman, B. T. Khuri-Yakub and S. S. Gambhir, *J. Am. Chem. Soc.*, 2010, **132**, 11264–11269.

- ChemComm Feature Article
- 114 L. A. Liotta, K. Tryggvason, S. Garbisa, I. Hart, C. M. Foltz and S. Shafie, *Nature*, 1980, 284, 67–68.
- 115 K. Kessenbrock, V. Plaks and Z. Werb, Cell, 2010, 141, 52-67.
- 116 G. Ku, M. Zhou, S. L. Song, Q. Huang, J. Hazle and C. Li, *ACS Nano*, 2012, **6**, 7489–7496.
- 117 Z. Zha, S. Zhang, Z. Deng, Y. Li, C. Li and Z. Dai, *Chem. Commun.*, 2013, 49, 3455–3457.
- 118 S. J. Byrne, Y. Williams, A. Davies, S. A. Corr, A. Rakovich, Y. K. Gun'ko, Y. R. Rakovich, J. F. Donegan and Y. Volkov, *Small*, 2007, 3, 1152–1156.
- 119 T. H. Shin, Y. Choi, S. Kim and J. Cheon, *Chem. Soc. Rev.*, 2015, 44, 4501–4516.
- 120 L. Xi, S. R. Grobmyer, G. Y. Zhou, W. P. Qian, L. Yang and H. B. Jiang, *J. Biophotonics*, 2014, 7, 401–409.
- 121 S. Del Vecchio, M. P. Stoppelli, M. V. Carriero, R. Fonti, O. Massa, P. Y. Li, G. Botti, M. Cerra, G. D'Aiuto and G. Esposito, et al., Cancer Res., 1993, 53, 3198–3206.
- 122 J. Yu, W. Y. Yin, X. P. Zheng, G. Tian, X. Zhang, T. Bao, X. H. Dong, Z. L. Wang, Z. J. Gu, X. Y. Ma and Y. L. Zhao, *Theranostics*, 2015, 5, 931–945.
- 123 J. Yu, C. Yang, J. D. S. Li, Y. C. Ding, L. Zhang, M. Z. Yousaf, J. Lin, R. Pang, L. B. Wei, L. L. Xu, F. G. Sheng, C. H. Li, G. J. Li, L. Y. Zhao and Y. L. Hou, *Adv. Mater.*, 2014, 26, 4114–4120.
- 124 A. K. Gupta, R. R. Naregalkar, V. D. Vaidya and M. Gupta, *Nanomedicine*, 2007, 2, 23–39.
- 125 S. Laurent and M. Mahmoudi, Int. J. Mol. Epidemiol. Genet., 2011, 2, 367–390.
- 126 X. Michalet, F. F. Pinaud, L. A. Bentolila, J. M. Tsay, S. Doose, J. J. Li, G. Sundaresan, A. M. Wu, S. S. Gambhir and S. Weiss, *Science*, 2005, 307, 538-544.
- 127 A. M. Smith, H. Duan, A. M. Mohs and S. Nie, Adv. Drug Delivery Rev., 2008, 60, 1226–1240.
- 128 E. V. Shashkov, M. Everts, E. I. Galanzha and V. P. Zharov, *Nano Lett.*, 2008, 8, 3953–3958.
- 129 E. Petryayeva, W. R. Algar and I. L. Medintz, Appl. Spectrosc., 2013, 67, 215–252.
- 130 H. S. Choi, W. Liu, P. Misra, E. Tanaka, J. P. Zimmer, B. I. Ipe, M. G. Bawendi and J. V. Frangioni, *Nat. Biotechnol.*, 2007, 25, 1165–1170.
- 131 S. L. Luo, E. L. Zhang, Y. P. Su, T. M. Cheng and C. M. Shi, Biomaterials, 2011, 32, 7127–7138.
- 132 J. O. Escobedo, O. Rusin, S. Lim and R. M. Strongin, *Curr. Opin. Chem. Biol.*, 2010, **14**, 64–70.
- 133 M. Sameiro and T. Goncalves, Chem. Rev., 2009, 109, 190-212.
- 134 T. Gorecki, G. Patonay, L. Strekowski, R. Chin and N. Salazar, J. Heterocycl. Chem., 1996, 33, 1871–1876.
- 135 X. J. Peng, F. L. Song, E. Lu, Y. N. Wang, W. Zhou, J. L. Fan and Y. L. Gao, *J. Am. Chem. Soc.*, 2005, **127**, 4170–4171.
- 136 L. C. Zhou, G. J. Zhao, J. F. Liu, K. L. Han, Y. K. Wu, X. J. Peng and M. T. Sun, J. Photochem. Photobiol., A, 2007, 187, 305–310.
- 137 Y. H. Lin, R. Weissleder and C. H. Tung, *Bioconjugate Chem.*, 2002, 13, 605–610.
- 138 M. L. Landsman, G. Kwant, G. A. Mook and W. G. Zijlstra, J. Appl. Physiol., 1976, 40, 575–583.
- 139 I. J. Fox, L. G. Brooker, D. W. Heseltine, H. E. Essex and E. H. Wood, *Proc. Staff Meet. Mayo Clin.*, 1957, 32, 478–484.
- 140 J. T. Alander, I. Kaartinen, A. Laakso, T. Patila, T. Spillmann, V. V. Tuchin, M. Venermo and P. Valisuo, *Int. J. Biomed. Imaging*, 2012, 2012, 940585.
- 141 L. B. Rowell, J. R. Blackmon and R. A. Bruce, J. Clin. Invest., 1964, 43, 1677–1690.
- 142 J. Zhong, S. Yang, X. Zheng, T. Zhou and D. Xing, *Nanomedicine*, 2013, 8, 903–919.
- 143 T. Desmettre, J. M. Devoisselle and S. Mordon, Surv. Ophthalmol., 2000, 45, 15–27.
- 144 W. M. Kuebler, J. Appl. Physiol., 2008, 104, 905-906.
- 145 R. Philip, A. Penzkofer, W. Baumler, R. M. Szeimies and C. Abels, J. Photochem. Photobiol., A, 1996, 96, 137–148.
- 146 C. Kim, K. H. Song, F. Gao and L. H. V. Wang, *Radiology*, 2010, 255, 442–450.
- 147 N. Beziere, N. Lozano, A. Nunes, J. Salichs, D. Queiros, K. Kostarelos and V. Ntziachristos, *Biomaterials*, 2015, 37, 415–424.
- 148 N. Lozano, Z. S. Al-Ahmady, N. S. Beziere, V. Ntziachristos and K. Kostarelos, *Int. J. Pharm.*, 2015, 482, 2-10.

- 149 X. Y. Chen, X. J. Peng, A. J. Cui, B. S. Wang, L. Wang and R. Zhang, J. Photochem. Photobiol., A, 2006, 181, 79–85.
- 150 S. Onoe, T. Temma, K. Kanazaki, M. Ono and H. Saji, J. Biomed. Opt., 2015, 20, 09006.
- 151 N. Sim, S. Gottschalk, R. Pal, M. Delbianco, O. Degtyaruk, D. Razansky, G. G. Westmeyer, V. Ntziachristos, D. Parker and A. Mishra, *Chem. Commun.*, 2015, 51, 15149–15152.
- 152 N. Sim and D. Parker, Chem. Soc. Rev., 2015, 44, 2122-2134.
- 153 F. M. Hamann, R. Brehm, J. Pauli, M. Grabolle, W. Frank, W. A. Kaiser, D. Fischer, U. Resch-Genger and I. Hilger, *Mol. Imaging*, 2011, 10, 258–269.
- 154 A. Mishra, Y. Jiang, S. Roberts, V. Ntziachristos and G. G. Westmeyer, Anal. Chem., 2016, 88, 10785–10789.
- 155 N. Beziere and V. Ntziachristos, J. Nucl. Med., 2015, 56, 323-328.
- 156 A. Dragulescu-Andrasi, S. R. Kothapalli, G. A. Tikhomirov, J. Rao and S. S. Gambhir, *J. Am. Chem. Soc.*, 2013, 135, 11015–11022.
- 157 H. Li, P. Zhang, L. P. Smaga, R. A. Hoffman and J. Chan, J. Am. Chem. Soc., 2015, 137, 15628–15631.
- 158 S. Guha, G. K. Shaw, T. M. Mitcham, R. R. Bouchard and B. D. Smith, *Chem. Commun.*, 2016, **52**, 120–123.
- 159 K. H. Song, E. W. Stein, J. A. Margenthaler and L. V. Wang, J. Biomed. Opt., 2008, 13, 054033.
- 160 M. Jeon, W. T. Song, E. Huynh, J. Kim, J. Kim, B. L. Helfield, B. Y. C. Leung, D. E. Goertz, G. Zheng, J. Oh, J. F. Lovell and C. Kim, J. Biomed. Opt., 2014, 19, 16005.
- 161 X. L. Liang, Z. J. Deng, L. J. Jing, X. D. Li, Z. F. Dai, C. H. Li and M. M. Huang, Chem. Commun., 2013, 49, 11029–11031.
- 162 J. Yao, K. Maslov, S. Hu and L. V. Wang, J. Biomed. Opt., 2009, 14, 054049.
- 163 G. Nie, H. J. Hah, G. Kim, Y. E. Lee, M. Qin, T. S. Ratani, P. Fotiadis, A. Miller, A. Kochi, D. Gao, T. Chen, D. A. Orringer, O. Sagher, M. A. Philbert and R. Kopelman, Small, 2012, 8, 884–891.
- 164 A. Ray, X. D. Wang, Y. E. K. Lee, H. J. Hah, G. Kim, T. Chen, D. A. Orringer, O. Sagher, X. J. Liu and R. Kopelman, *Nano Res.*, 2011, 4, 1163–1173.
- 165 N. Y. Kang, S. J. Park, X. W. E. Ang, A. Samanta, W. H. P. Driessen, V. Ntziachristos, K. O. Vasquez, J. D. Peterson, S. W. Yun and Y. T. Chang, *Chem. Commun.*, 2014, 50, 6589–6591.
- 166 P. Allavena and A. Mantovani, Clin. Exp. Immunol., 2012, 167, 195-205.
- 167 F. F. An, Z. J. Deng, J. Ye, J. F. Zhang, Y. L. Yang, C. H. Li, C. J. Zheng and X. H. Zhang, ACS Appl. Mater. Interfaces, 2014, 6, 17985–17992.
- 168 D. Razansky, M. Distel, C. Vinegoni, R. Ma, N. Perrimon, R. W. Koster and V. Ntziachristos, *Nat. Photonics*, 2009, 3, 412–417.
- 169 D. Razansky, C. Vinegoni and V. Ntziachristos, *Phys. Med. Biol.*, 2009, 54, 2769–2777.
- 170 G. S. Filonov, A. Krumholz, J. Xia, J. J. Yao, L. H. V. Wang and V. V. Verkhusha, *Angew. Chem., Int. Ed.*, 2012, 51, 1448–1451.
- 171 L. Li, R. J. Zemp, G. Lungu, G. Stoica and L. H. V. Wang, J. Biomed. Opt., 2007, 12, 020504.
- 172 A. Krumholz, S. J. VanVickle-Chavez, J. J. Yao, T. P. Fleming, W. E. Gillanders and L. H. V. Wang, *J. Biomed. Opt.*, 2011, 16, 080503.
- 173 R. J. Paproski, A. E. Forbrich, K. Wachowicz, M. M. Hitt and R. J. Zemp, *Biomed. Opt. Express*, 2011, 2, 771–780.
- 174 Y. Jiang, F. Sigmund, J. Reber, X. L. Deán-Ben, S. Glasl, M. Kneipp, H. Estrada, D. Razansky, V. Ntziachristos and G. G. Westmeyer, Sci. Rep., 2015, 5, 11048.
- 175 J. Stritzker, L. Kirscher, M. Scadeng, N. C. Deliolanis, S. Morscher, P. Symvoulidis, K. Schaefer, Q. Zhang, L. Buckel, M. Hess, U. Donat, W. G. Bradley, V. Ntziachristos and A. A. Szalay, *Proc. Natl. Acad. Sci. U. S. A.*, 2013, 110, 3316–3320.
- 176 R. J. Paproski, A. Heinmiller, K. Wachowicz and R. J. Zemp, *Sci. Rep.*, 2014, 4, 11048.
- 177 J. T. Oh, M. L. Li, H. F. Zhang, K. Maslov, G. Stoica and L. H. V. Wang, J. Biomed. Opt., 2006, 11, 34032.
- 178 L. Kirscher, X. L. Dean-Ben, M. Scadeng, A. Zaremba, Q. Zhang, C. Kober, T. F. Fehm, D. Razansky, V. Ntziachristos, J. Stritzker and A. A. Szalay, *Theranostics*, 2015, 5, 1045–1057.
- 179 A. Premkumar, F. Marincola, J. Taubenberger, C. Chow, D. Venzon and D. Schwartzentruber, *J. Magn. Reson. Imaging*, 1996, 6, 190–194.
- 180 J. O. DeJordy, P. Bendel, A. Horowitz, Y. Salomon and H. Degani, J. Magn. Reson. Imaging, 1992, 2, 695–700.
- 181 A. P. Jathoul, J. Laufer, O. Ogunlade, B. Treeby, B. Cox, E. Zhang, P. Johnson, A. R. Pizzey, B. Philip, T. Marafioti, M. F. Lythgoe, R. B. Pedley, M. A. Pule and P. Beard, *Nat. Photonics*, 2015, 9, 239–246.

- 182 Y. Liu, L. Hong, V. R. Kempf, K. Wakamatsu, S. Ito and J. D. Simon, Pigm. Cell Res., 2004, 17, 262-269.
- 183 A. Samokhvalov, Y. Liu and J. D. Simon, Photochem. Photobiol., 2004, 80, 84-88.
- 184 J. J. Yao, A. A. Kaberniuk, L. Li, D. M. Shcherbakova, R. Y. Zhang, L. D. Wang, G. Li, V. V. Verkhusha and L. H. V. Wang, Nat. Methods, 2016, 13, 67-73.
- 185 A. C. Stiel, X. L. Dean-Ben, Y. Jiang, V. Ntziachristos, D. Razansky and G. G. Westmeyer, Opt. Lett., 2015, 40, 367-370.
- X. L. Deán-Ben, G. Sela, A. Lauri, M. Kneipp, V. Ntziachristos, G. G. Westmeyer, S. Shoham and D. Razansky, Light: Sci. Appl., 2016, 5, e16201.
- 187 A. Jacobs, J. Voges, R. Reszka, M. Lercher, A. Gossmann, L. Kracht, C. Kaestle, R. Wagner, K. Wienhard and W. D. Heiss, Lancet, 2001,
- 188 J. H. Kang and J. K. Chung, J. Nucl. Med., 2008, 49, 164s–179s.
- 189 X. Huang and M. A. El-Sayed, J. Adv. Res., 2010, 1, 13-28.
- 190 Y. Wang and L. V. Wang, J. Biomed. Opt., 2012, 17, 086007.
- 191 Y. Li, A. Forbrich, J. H. Wu, P. Shao, R. E. Campbell and R. Zemp, Sci. Rep., 2016, 6, 22129.
- 192 S. Tzoumas, A. Kravtsiv, Y. Gao, A. Buehler and V. Ntziachristos, IEEE Trans. Med. Imaging, 2016, 35, 2534-2545.
- 193 V. Ermolayev, X. L. Dean-Ben, S. Mandal, V. Ntziachristos and D. Razansky, Eur. J. Radiol., 2016, 26, 1843–1851.
- 194 M. van Oosten, T. Schafer, J. A. Gazendam, K. Ohlsen, E. Tsompanidou, M. C. de Goffau, H. J. Harmsen, L. M. Crane, E. Lim, K. P. Francis, L. Cheung, M. Olive, V. Ntziachristos, J. M. van Dijl and G. M. van Dam, Nat. Commun., 2013, 4, 2584.
- 195 M. V. Marshall, D. Draney, E. M. Sevick-Muraca and D. M. Olive, Mol. Imaging Biol., 2010, 12, 583-594.
- 196 A. G. Terwisscha van Scheltinga, G. M. van Dam, W. B. Nagengast, V. Ntziachristos, H. Hollema, J. L. Herek, C. P. Schroder, J. G. Kosterink, M. N. Lub-de Hoog and E. G. de Vries, J. Nucl. Med., 2011, 52, 1778-1785.
- 197 C. Kim, T. N. Erpelding, L. Jankovic and L. V. Wang, Philos. Trans. R. Soc., A, 2011, 369, 4644-4650.
- 198 C. Li, A. Aguirre, J. Gamelin, A. Maurudis, Q. Zhu and L. V. Wang, J. Biomed. Opt., 2010, 15, 010509.
- 199 L. Song, C. Kim, K. Maslov, K. K. Shung and L. V. Wang, Med. Phys., 2009, 36, 3724-3729.

- 200 T. D. MacDonald, T. W. Liu and G. Zheng, Angew. Chem., Int. Ed., 2014, 53, 6956-6959.
- 201 H. Yuan, C. G. Khoury, H. Hwang, C. M. Wilson, G. A. Grant and T. Vo-Dinh, Nanotechnology, 2012, 23, 075102.
- 202 C. Kim, H. M. Song, X. Cai, J. Yao, A. Wei and L. V. Wang, J. Mater. Chem., 2011, 21, 2841-2844.
- 203 S. Liang, C. Li, C. Zhang, Y. Chen, L. Xu, C. Bao, X. Wang, G. Liu,
- F. Zhang and D. Cui, *Theranostics*, 2015, 5, 970–984. 204 S. J. Yoon, S. Mallidi, J. M. Tam, J. O. Tam, A. Murthy, K. P. Johnston, K. V. Sokolov and S. Y. Emelianov, Opt. Lett., 2010, 35, 3751-3753.
- 205 S. J. Yoon, A. Murthy, K. P. Johnston, K. V. Sokolov and S. Y. Emelianov, Opt. Express, 2012, 20, 29479-29487.
- 206 D. Pan, M. Pramanik, A. Senpan, J. S. Allen, H. Zhang, S. A. Wickline, L. V. Wang and G. M. Lanza, FASEB J., 2011, 25, 875-882.
- 207 D. Pan, M. Pramanik, S. A. Wickline, L. V. Wang and G. M. Lanza, Contrast Media Mol. Imaging, 2011, 6, 378-388.
- 208 J. Lin, S. Wang, P. Huang, Z. Wang, S. Chen, G. Niu, W. Li, J. He, D. Cui, G. Lu, X. Chen and Z. Nie, ACS Nano, 2013, 7, 5320-5329.
- 209 W. Lu, M. P. Melancon, C. Xiong, Q. Huang, A. Elliott, S. Song, R. Zhang, L. G. Flores, 2nd, J. G. Gelovani, L. V. Wang, G. Ku, R. J. Stafford and C. Li, Cancer Res., 2011, 71, 6116-6121.
- 210 H. Xie, P. Diagaradjane, A. A. Deorukhkar, B. Goins, A. Bao, W. T. Phillips, Z. Wang, J. Schwartz and S. Krishnan, Int. J. Nanomed., 2011, 6, 259-269.
- 211 M. L. Li, J. C. Wang, J. A. Schwartz, K. L. Gill-Sharp, G. Stoica and L. V. Wang, J. Biomed. Opt., 2009, 14, 010507.
- 212 D. J. Grootendorst, J. Jose, R. M. Fratila, M. Visscher, A. H. Velders, B. Ten Haken, T. G. Van Leeuwen, W. Steenbergen, S. Manohar and T. J. Ruers, Contrast Media Mol. Imaging, 2013, 8, 83-91.
- 213 C. Wang, X. X. Ma, S. Q. Ye, L. Cheng, K. Yang, L. Guo, C. H. Li, Y. G. Li and Z. Liu, Adv. Funct. Mater., 2012, 22, 2363-2375.
- 214 Y. W. Wang, Y. Y. Fu, Q. L. Peng, S. S. Guo, G. Liu, J. Li, H. H. Yang and G. N. Chen, J. Mater. Chem. B, 2013, 1, 5762-5767.
- 215 D. H. Hu, J. N. Zhang, G. H. Gao, Z. H. Sheng, H. D. Cui and L. T. Cai, Theranostics, 2016, 6, 1043-1052.
- 216 X. Liu, W. C. Law, M. Jeon, X. L. Wang, M. X. Liu, C. Kim, P. N. Prasad and M. T. Swihart, Adv. Healthcare Mater., 2013, 2, 952-957.